

The Impact of Ice-Supersaturated-Regions (ISSR) and Cirrus clouds on Radiation

Fabian Fusina

Institute for Atmospheric and Climatic Science - ETH Zurich
Remote Sensing Laboratory, Institute of Geography - University of Zurich

May 2, 2007

Abstract

In this thesis I investigate the radiative impact of ice supersaturated regions (ISSRs, i.e. cloud free air masses in the upper troposphere in the status of supersaturation with respect to ice) and thin cirrus clouds. For this purpose I use corrected radiosonde data obtained from routine measurements over the meteorological observatory Lindenberg, Germany. The radiative effect of the measured ice supersaturation is determined. By constructing an idealized profile from the measurement data, the radiative properties of ISSRs and thin cirrus clouds containing ice supersaturation were studied. The impact of ISSRs on the surface forcing is negligible but locally, within the vertical profile there could be changes in the heating rates up to 1 K/day for typical values of relative humidity with respect to ice of 130% compared to the saturated profiles. This is important for the local dynamics within the supersaturated layers. Additionally, at the top of the atmosphere there is a remarkable change in the outgoing longwave radiation due to the enhanced water vapor content inside ISSRs. The radiative impact of thin cirrus clouds is much stronger. Thin cirrus clouds influence both, the surface budget, top of the atmosphere radiation and vertical profile. The impact depends strongly on cloud ice content and the size of the ice crystals. Thin cirrus clouds also influence the accuracy of some remote sensing sensors.

Contents

1	Introduction	3
2	Basics	6
2.1	Global Radiation Transfer	6
2.2	Ice Supersaturated Regions	12
3	Data Description	14
3.1	Radiosonde Data	14
3.2	Data Processing	16
3.3	Radiation Model	21
4	Results and Discussion	25
4.1	Radiosonde Profiles	25
4.2	Idealized ISSR Profiles and its impact on radiation	29
4.3	Radiative Impact on Local ISSR Dynamics	38
4.4	Thin Cirrus Clouds and its Impact on Radiation	41
4.5	Impact of incorrectly formed cirrus clouds in GCMs	46
4.6	The Impact on Remote Sensing	47
5	Conclusions and Outlook	52

Chapter 1

Introduction

The existence of cloud-free air masses that are supersaturated with respect to (wrt) ice in the upper troposphere or lowermost stratosphere is known since almost 60 years. Glückauf (1945) found from hygrometer data obtained over Southern England that very high ice supersaturation (i.e. values up to 160% relative humidity wrt ice) occurs frequently in the upper troposphere. However, probably the first observations of ice supersaturation were made by Alfred Wegener during his second expedition to Greenland in 1911/12 (c.f. Wall, 1942) who recognized that moist breathing of his horses produced small ice crystals. These insights from the first part of the 20th century were neglected for many years, and measurements reporting ice supersaturation often were termed as errors. During the last decade the existence of air masses in the status of supersaturation was proved by many measurements with a variety of different measurement techniques (e.g. Jensen et al., 1998; Vay et al., 2000; Ovarlez et al., 2000). Theoretical considerations are consistent with the existence of ice supersaturation because ice crystals form at very high supersaturations, the exact freezing thresholds depends on the formation mechanism (homogeneous freezing of solution droplets or heterogeneous nucleation) (e.g. Koop et al., 2000; De Mott et al., 2003).

The properties and global distributions of ice supersaturated regions (ISSRs) were discovered during the last years (e.g. Spichtinger et al., 2003a,b; Gettelman et al., 2006). However, the radiative impact of ISSRs was never discussed. This is surprising because in ISSRs the water vapor content is much higher than in the subsaturated environment. Water vapor is a very effective greenhouse gas and it is well known that it provides a positive feedback to the forcing from well-mixed greenhouse gases (see e.g. Forster and Gregory, 2006; Soden et al., 2005). ISSRs are relatively frequent in the

upper troposphere. They occur 20-30% of the time in cloud free airmasses over the North Atlantic. Because of the huge horizontal extensions of ISSRs (mean 150 ± 250 km, Gierens and Spichtinger, 2000) there is a substantial amount of cloud free air masses with enhanced water vapor content.

ISSRs are the potential formation regions of cirrus clouds and persistent contrails. These clouds are important modulators of the radiation budget. The contribution of thin cirrus clouds to Earth' radiation budget is not well known, but it is assumed that they contribute to a net heating of the Earth-Atmosphere system (e.g. Chen et al., 2000).

There is a principle difference in the radiative impact of ISSRs and cirrus clouds (see fig.1.1): In case of a cloud free ice supersaturated layer the incoming solar radiation passes through the supersaturation layer with hardly any absorption. On the other hand the outgoing longwave radiation is partly absorbed by the enhanced water vapor inside the ISSR. Hence, ISSRs have only a significant effect on the longwave radiation. For thin cirrus clouds the picture changes a bit. The incoming solar radiation is (partly) scattered at the ice crystals in the cirrus layer, and also the outgoing longwave radiation is absorbed by the ice crystals. If there is supersaturation inside the cirrus cloud layer (which is frequently found in many measurements, see below) the effect of absorbing longwave radiation due to enhanced water vapor also contributes to the radiative effect on thin cirrus clouds. Although the existence

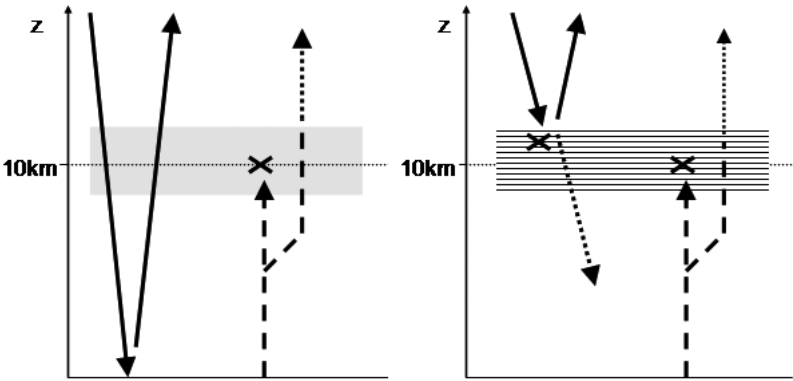


Figure 1.1: Radiative impact of ISSRs and thin cirrus clouds. Left: ISSRs; the incoming solar radiation is not affected by ISSRs, whereas the outgoing infrared radiation is absorbed by the enhanced water vapor concentration. Right: thin cirrus clouds; here, both the solar and infrared radiation are affected by the ice crystals

of ice supersaturated regions was proved by theoretical considerations and measurements and ice crystal nucleation takes place at (high) ice supersaturations, in general circulation models (GCMs) usually ice clouds are formed at ice saturation. There are only two versions of climate models which allows ice supersaturation (Lohmann and Kärcher, 2002; Gettelman et al., 2006) and one version of the ECMWF numerical weather model (Tompkins et al., 2007). However, it is not clear how large the error in the radiation budget will be if cirrus clouds were formed incorrectly at saturation and not from physical principles.

In this thesis I want to investigate the radiative impact of ISSRs and thin cirrus clouds as well for the radiation budget as for the vertical heating rates. For this purpose I use radiosonde data which were used before for investigations of ISSRs by Spichtinger et al. (2003a) and also idealized atmospheric profiles. Also the impact of ISSRs and thin cirrus clouds on remote sensing applications will be discussed.

Chapter 2

Basics

2.1 Global Radiation Transfer

The solar radiation and the conversion of this energy in the systems of ocean, solid earth surface and the atmosphere are the main forcing mechanisms of the atmospheres behavior. Only 0.0004% of the whole energy production of the sun reach the earths surface with a wavelength spectrum from 1nm up to 100m. The maximum of the energy-distribution is in the visble range of the spectrum (between 0.36 and 0.76 μm wavelength). The energyflux reaching the earth outside the atmosphere, averaged over the whole path of the earth for one year, is called the solar sonstant S_0 . It represents the total integrated irradiance over the entire spectrum. The value of the solar constant is:

$$S_0 = 1367 \pm 3 [Wm^{-2}]$$

Averaged over the whole terrestrial globe (day- and night-side), the value reduces to $S = 342 [Wm^{-2}]$. Over a long timescale, the solar constant is not really constant. It varies by some tenth of a percent.

When the solar radiation enters the atmosphere, it is exposed to different effects. Mainly, the beam becomes absorbed and scattered by the gases and particles of the atmosphere (extinction). The wavelength and also the amount of the absorption depends on the gases, which the corresponding layer of the atmosphere contains (Figure 2.1). Atomic and molecular oxygen (O_2) and nitrogen absorb very shortwave radiation, effectively blocking radiation with wavelengths lower than 190 nm. When molecular oxygen in the atmosphere absorbs short wave ultraviolet radiation, it photodissociates. This leads to the production of ozone (O_3). Ozone strongly absorbs longer wavelength ultraviolet in the Hartley band from 200 - 300 nm and weakly

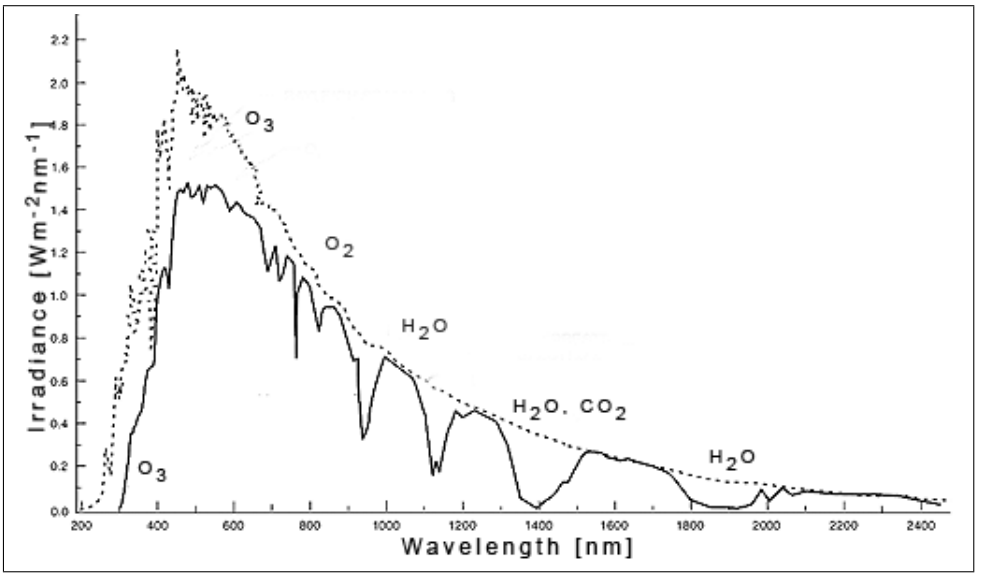


Figure 2.1: Global Radiation - solid line: spectrum at sea level, dashed line: extraterrestrial spectrum

absorbs visible radiation. The ozone layer absorbs UV up to 280 nm and (with atmospheric scattering) shapes the UV edge of the terrestrial solar spectrum (e.g. Molina et al. (1986)). Water vapor, carbon dioxide, and to a lesser extent, oxygen, selectively absorb in the near- and thermal-infrared. Wavelength dependent Rayleigh scattering and scattering from aerosols and other particulates, including water droplets, also change the spectrum of the radiation that reaches the ground.

The spectrum at the ground has several components: Direct radiation, which has no interaction with the atmosphere, diffuse radiation, which is scattered by the components of the atmosphere and reflected radiation from the surroundings (depends on the albedo of the surface). The total amount of this irradiance is called global radiation. - For a typical cloudless atmosphere at the equator (zenith angle = 0°) the $1367 [W m^{-2}]$ reaching the outer atmosphere is reduced to ca. $1050 [W m^{-2}]$ direct beam radiation, and ca. $1120 [W m^{-2}]$ global radiation on a horizontal surface at ground level (e.g. Halthore et al. (1997b)).

On the other hand, the earth's surface emits a part of the absorbed energy back to the atmosphere. This kind of radiation will be called "longwave radiation" in this thesis. According to the Planck-function about black-body radiation (Equation 2.1), the wavelength of the peak of the energy-

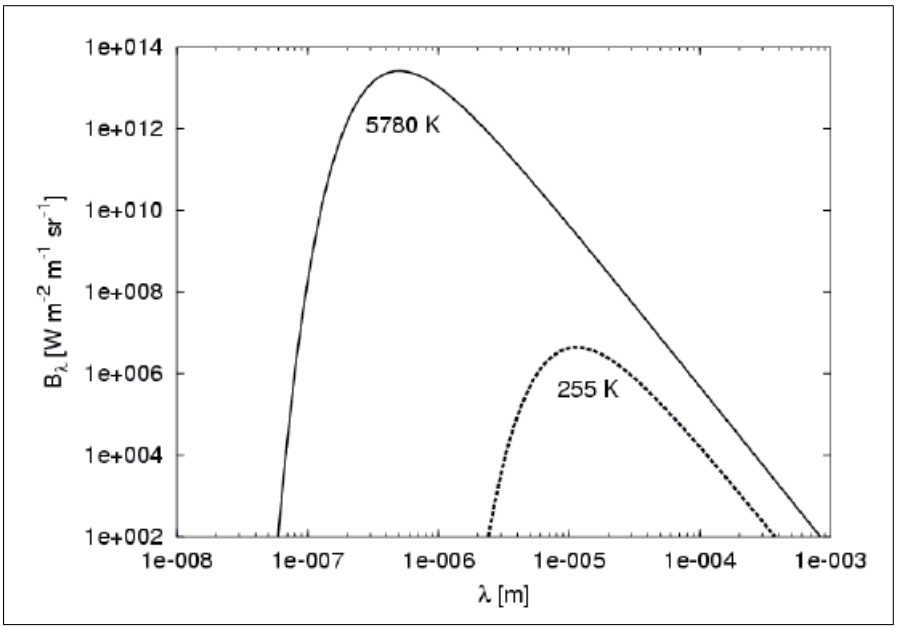


Figure 2.2: Blackbody Radiation - solid line: earth, dashed line: sun, P. Calanca IAC ETH

distribution is much longer, than those of the direct sun radiation (Figure 2.2). This shift is described by the Wien's displacement law (Equation 2.3).

$$B_{\lambda}(T) = 2hc^2\lambda^{-5} \left(\exp\left(\frac{hc}{\lambda kT}\right) - 1 \right)^{-1} \quad [Wm^{-2}m^{-1}sr^{-1}] \quad (2.1)$$

Where c is the speed of sound, h the Planck constant, k the Boltzmann constant and T the absolute Temperature. After integration over all wavelengths follows:

$$B(T) = \frac{\sigma T^4}{\pi} \quad (2.2)$$

The Wien's displacement law is written as:

$$\lambda_{max} T = 2.898 \cdot 10^{-3} [^{\circ}K \cdot m] \quad (2.3)$$

The whole radiation transfer in the atmosphere can be concluded into Figure 2.3. This graphic shows the radiation fluxes averaged over all latitudes. The net radiation budget TOA averaged over all latitudes, which is just the difference between incoming and outgoing radiation, is 0 (the shortcut "TOA" means "at the top of the atmosphere" and will be used from now

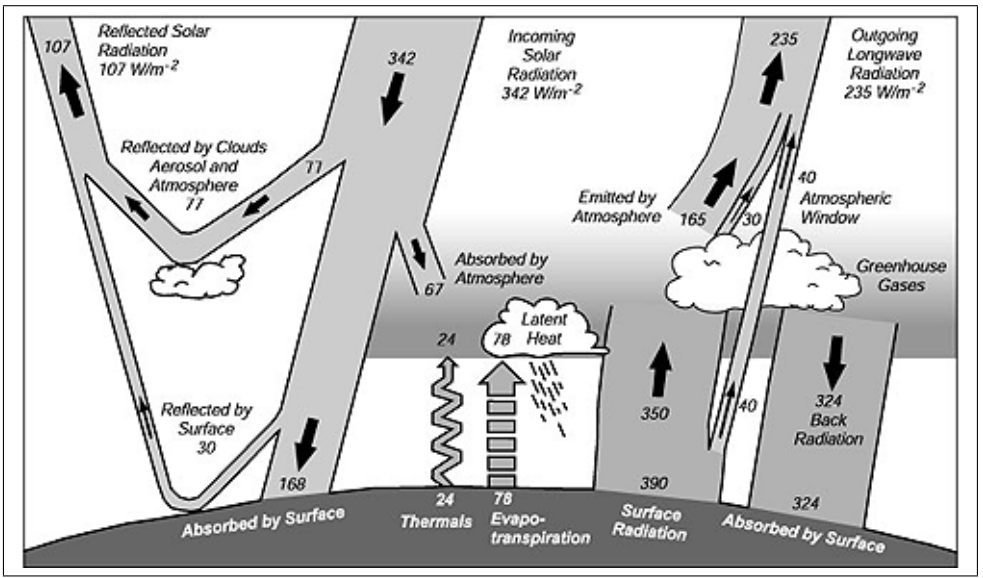


Figure 2.3: Global Radiation Transfer

on). Some areas of the world absorb more energy than they reemit, they should become warmer and warmer (tropics). On the contrary, areas for which radiative balance is negative should become colder and colder (higher latitudes). This does not happen because the atmosphere and the oceans are continuously transporting heat from equator to the poles. The radiation fluxes TOA are shown in the figures 2.4 and 2.5. Later in this thesis, we will look at atmospheric profiles of Lindenberg (Germany) at a latitude of 52° . In figure 2.5 it is evident, that we can estimate a negative flux budget at this spot. All following model studies are based on a solar zenith angle of 50° . The solar zenith angle (θ) (equation 2.4) can be defined as the angle between the perpendicular line up in the sky and the solar position. It depends on the geographical latitude (ϕ), the solar declination (δ) (depends on the season) and the hour angle (ω) (depends on the daytime).

$$\theta = \arccos(\sin\phi \sin\delta + \cos\phi \cos\delta \cos\omega) \quad (2.4)$$

Since the main goal of this thesis is to determine the radiative properties of ISSRs and cirrus clouds, we are mostly interested in the scattering and absorbing processes, which influence the radiation on the way down to the earth's surface, and again on the way back to the space. For this study, I can distinguish two cases. The first case is in cloudless conditions. Our sun

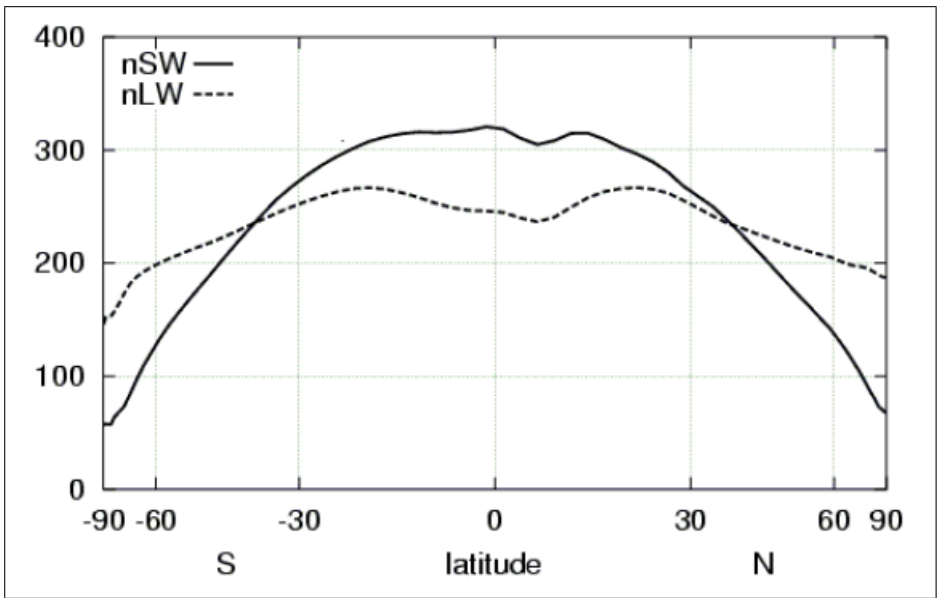


Figure 2.4: Radiation flux TOA - solid line: shortwave radiation [$W m^{-2}$], dashed line: longwave radiation [$W m^{-2}$], P. Calanca IAC ETH

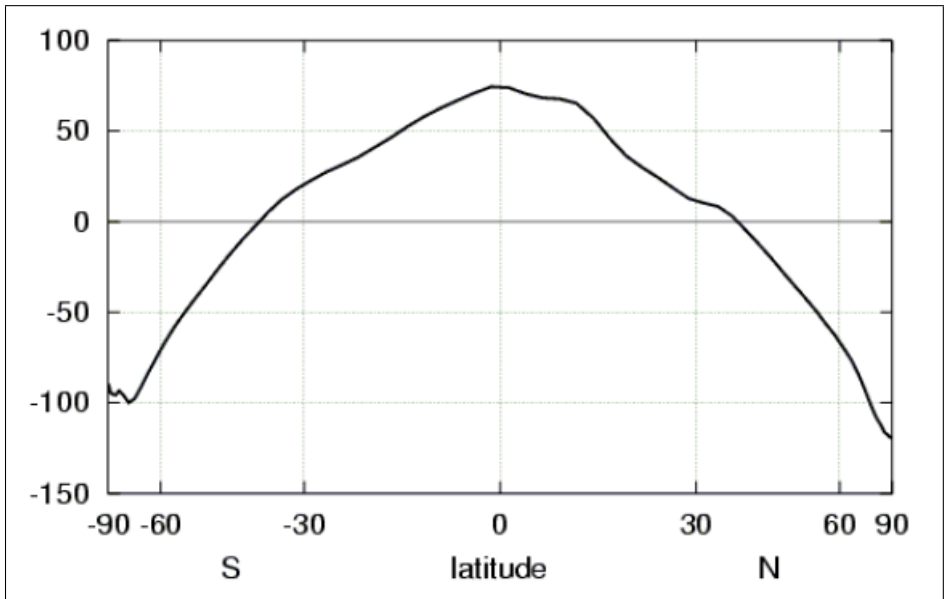


Figure 2.5: Net radiation flux TOA [$W m^{-2}$], P. Calanca IAC ETH

beam is only absorbed by trace gases of the atmosphere, mainly by water-vapor, which is the most important greenhouse gas in the atmosphere. By varying the partial pressure of water vapor on certain atmosphere layers, we can observe very specific changes of the radiation transfer. Since ice supersaturated regions contain more than the normal limit of 100% relative humidity, their impact on radiation should be very interesting and not negligible. In the other case, we look at atmospheric profiles, which also contain layers contaminated with cirrus clouds. In combination with the trace gas absorption, we now have also scattering and absorption on ice crystals in the cirrus cloud. The radiative absorption and scattering properties of ice crystals are very complex problems, which will be discussed later in this thesis.

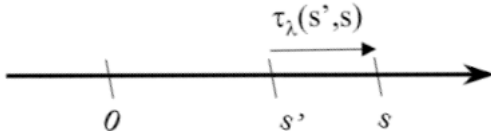
In contrast to the cloudless case, the cloud covered atmosphere has an optical depth greater than 0. The optical depth τ is defined as the integration of an extinction coefficient k_λ and the density of a medium (ice crystals in our case) over the path length (Equation 2.5). Because the extinction coefficient k_λ depends on the wavelength λ , the optical depth τ is also a function of λ . The transmissivity T_λ of an atmosphere layer with the thickness s is equivalent with the ratio between the outgoing (N_λ) and the incoming radiation ($N_{\lambda 0}$) intensity. This statement follows out of the Beer-Bouguer-Lambert Law (Equation 2.6).

$$\tau_\lambda = \int_0^s k_\lambda \rho ds \quad ; \quad T_\lambda = e^{-\tau_\lambda} = \frac{N_\lambda}{N_{\lambda 0}} \quad (2.5)$$

$$N_\lambda(s) = N_{\lambda 0} \cdot \exp\left(-k_\lambda \int_0^s \rho ds\right) \quad (2.6)$$

It is evident, that the same amount of energy which has been absorbed should be reemitted again. We can combine now the laws for the blackbody radiation and the absorption to the Schwarzschild-Equation:

$$N_\lambda(s) = N_{\lambda 0} e^{-\tau_\lambda(0,s)} + \int_0^s B_\lambda(T(s')) e^{-\tau_\lambda(s',s)} k_\lambda \rho ds' \quad (2.7)$$



2.2 Ice Supersaturated Regions

It is hard to describe an ice supersaturated region (ISSR) with a strictly sharp definition. We could call it a "cloud free ice-supersaturated region", which means that the relative humidity with respect to ice has to be $> 100\%$. The inaccuracy in this definition is, that it is very hard to detect, if a layer with an embedded supersaturation is really cloudfree. Perhaps there is only one single ice crystal per squaremeter, which blasts our whole definition. In this case, every measurement technique would be overstrained. Therefore, we have to use a more practical definition, which includes the measurement accuracy: "a supersaturated region, where a certain measurement device has no evidence of the existence of ice". It follows that the boarder between an ISSR and a thin cirrus cloud is very smooth, especially for subvisible cirrus (a cirrus cloud with a optical depth in the visible spectrum $\tau_{vis} < 0.03$). In fact we don't have to worry about this quit fuzzy definition, because before a subvisible cirrus (SVC) has been formed, an ISSR must have preexisted. ISSRs are mostly located in the upper troposphere near the tropopause at altitudes of about 8 to 12 km. Their thickness and maximum amount of water vapor can vary allot. It has to be considered, that most cirrus clouds have been built out of an ISSR. That means that cloud formation is a possible evolution of an ISSR. Statistics about their shape and properties are shown in the next chapters. There are a lot of reasons, why ISSRs, their distribution (climatology) and their properties are so interesting:

- ISSRs are neglected in most weather- and climate-models (GCMs) (except for those two described in the Introduction), where ice nucleation normally takes place at saturation. Out of this follows that for some cases, incorrectly formed cirrus clouds occupy a layer instead of an ISSR. Since cirrus clouds are a very sensitive modulator of the radiative budged, unexpected error could propagate.
- Because supersaturation resp. ISSRs are not considered within the most climate-models, it is not possible to say how ISSRs behave in changed climate conditions. The same also concerns to cirrus clouds and their impact on radiation.
- The high amount of relative humidity inside ISSRs may react more sensitive and intense on climate change than regions with medium relative humidities. Therefore, the monitoring of ISSRs could be a "early warning system" of possible climate changes and extreme weather phenomenas.

- Persistent contrails (contrails with a lifetime of more than 10 minutes) are only built inside ISSRs. Because the air traffics influence on climate change is dominated by contrails, it would be a goal to avoid their evolution. To achieve that, numeric weather forecast models should take ISSRs into account.

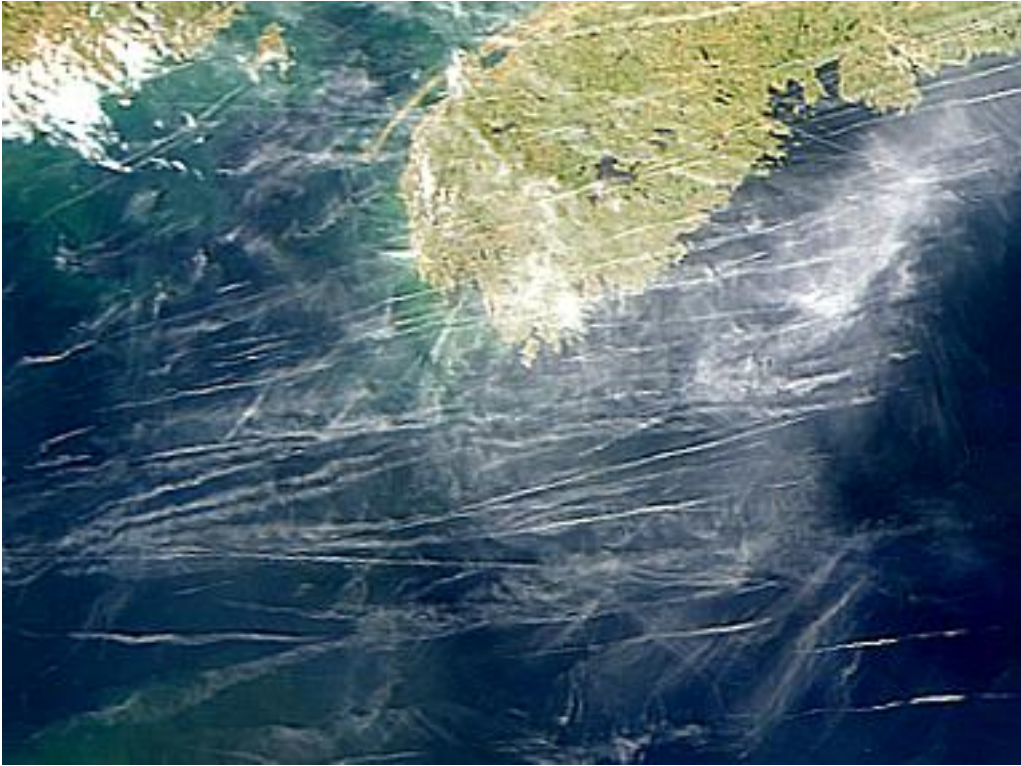


Figure 2.6: Persistent contrails over "Nova Scotia" Canada, NASA/GSFC Orbimage

Chapter 3

Data Description

3.1 Radiosonde Data

The first part of this thesis includes the analysis of radiosonde data, which have been obtained from routine ascents of Vaisala RS 80A radiosonde at the meteorological observatory Lindenberg, Germany. The usage of the standard radiosonde RS 80A with "humicap" humidity-sensors (capacitive sensors) is usually afflicted with errors in the low temperature range $T \leq -30^\circ\text{C}$, which results in a tremendous underestimation of the relative humidity with respect to ice. The research group of Dr. Ulrich Leiterer has developed a method to minimize the error, especially the underestimation of the relative humidity down to a acceptable value of 1.9% RH (relative humidity, mean standart deviation). This method is based on the comparison with the research-radiosonde RS 90, which obtains a higher accuracy of $\pm 1\%$ RH. Because of the much higher cost of this research-radiosonde it is used less then the older RS 80A. Although it should be noted that the amount of supersaturation is still markedly unterestimated: The maximum values are always lower than 140% RH_i (relative humidity wrt ice). Unfortunately, there is no direct comparison of corrected RS 80A profiles with other in situ measurements like frost point hygrometers of tunable diode lase instruments. Nevertheless, we know from in situ observations with other measurement techniques (i.e. from the MOSAIC-Project, Measurement of OZone and wAter vapour by Airbus In-service airCraft (e.g. Marengo et al., 1998)), that in the mid latitude values of RH_i up to 160-170% are possible and quite frequently (e.g. Jensen et al., 1998; Comstock et al., 2004).

I use data from the time period February, 2000 until April, 2001 for the standardized dates 00, 06, 12 and 18 UTC, this results in 1563 vertical profiles.

Following variables are measured by the sonde: temperature (T), pressure (p), altitude (z) and relative humidity with respect to water. Every measurement value corresponds to the mean value of 10 measurements within 10 seconds; together with the mean vertical upward velocity of the sonde of about 5 m/s this results into a vertical resolution of about 50 meters. All variables are available over a region from the ground up to the 100 hPa pressure layer, which corresponds to an altitude of about 15km above sea level (ASL). This raw data will later be proceeded to variables, which are usable for a statistical screening. More about that in the next section.

3.2 Data Processing

First of all, the high resolution data were interpolated polynomially on a fixed vertical grid with spacing of 200 meters. I achieve this with a polynomial interpolation method using MATLAB. To get the best results, the cubic-spline-interpolation has been chosen. It preserves monotonicity and the shape of the data most precisely. An example of an interpolated part of a relative humidity profile is shown in figure 3.1. The increasing of the resolution is necessary because the used GCM radiation model is designed for coarse vertical resolutions.

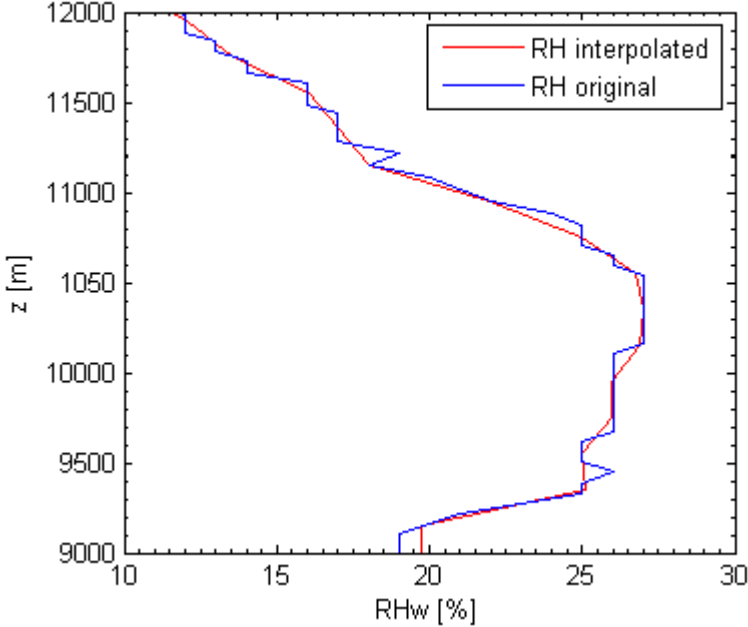


Figure 3.1: Relative humidity wrt water profile polynomial interpolated to a vertical resolution of 200m

Additionally, I only use vertical profiles with a complete recording from the surface to an altitude of approximately 15km. So every profile which includes some inaccuracies or missing data during the ascent will be sorted out. The detection of ISSRs has been carried out as in Spichtinger et al. (2003a): A radiosonde crossing an ensemble of supercooled water droplets would report $RH = 100\%$ which implies certainly ice supersaturation but this is neither an ISSR nor a cirrus cloud. Hence, a “dynamical” criterion to

register an ISSR is used. Its bottom temperature T_{lower} needs to be lower than $-30^{\circ}C$ and simultaneously its top temperature T_{upper} needs to be lower than $-35^{\circ}C$. This criterion avoids counting profiles containing supercooled water, but it is not a cloud clearing, i.e. the profiles could be contaminated with cirrus clouds. This is one of the big inaccuracies we have, while using radiosonde data. In the worst case, a thin cirrus cloud is mistakenly flagged as a true ISSR. We could prevent this problem by using a cloud-clearing procedure with Meteosat data. But for this thesis, it would be too time-consuming (We have more than 1500 different measuring-events!). For my first investigation I now assume that all these layers are cloud free. Using this criterion 401 ISSRs in 1563 vertical profiles are found. From these I only use single layer cases for further investigation, 293 out of the original number of ISSRs are single layer cases. The reason why I neglect the multi-layer ISSRs is, that it is too early to investigate some more complex and advanced cases before we understand the basics. This topic could be interesting in the future. More statistics will be discussed later in this thesis.

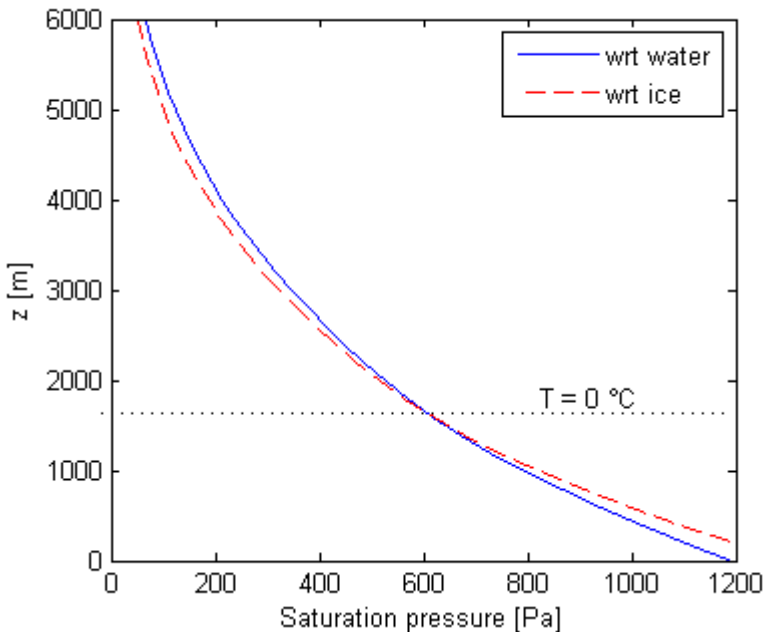


Figure 3.2: Saturation pressure wrt water and wrt ice

Furthermore the raw data is now being developed into typical variables, which are used in the atmospheric science. In this thesis, I will use the

relative humidity with respect to (wrt) ice to characterize the state of saturation/supersaturation. We can calculate now the relative humidity wrt ice (RH_i) using:

$$RH_i = RH \cdot \frac{p_{sat,w}(T)}{p_{sat,i}(T)} \quad (3.1)$$

Furthermore, $p_{sat,w}$ stands for the watervapor saturation-pressure over water, $p_{sat,i}$ for the saturation-pressure over ice. Those saturation pressures are calculated using the formula by Sonntag [1994], as in Spichtinger et al. (2003a). The specific humidity q can be calculated using following equation:

$$q = \frac{RH}{100\%} \cdot \frac{\epsilon \cdot p_{sat,w}(T)}{p} \quad (3.2)$$

whereby $\epsilon = \frac{R_d}{R_v}$ is the ration between the gas constants of dry air (R_d) and watervapor (R_v). $\epsilon = 0.662$. Additionally the unit of q is $\frac{kg}{kg}$.

The reason why I use the relative humidity wrt ice instead of the relative

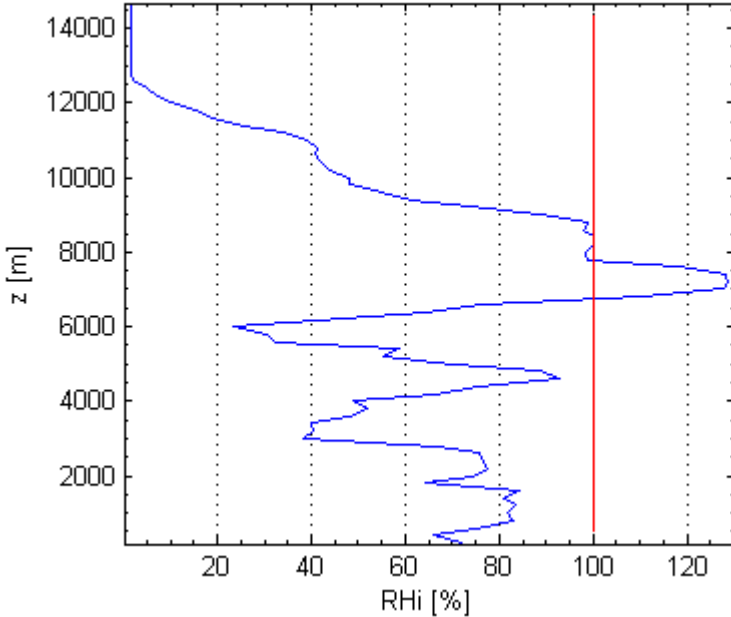


Figure 3.3: Relative humidity wrt ice profile, containing a single layer ISSR with max RH_i \approx 130, obtained from routine ascent of Vaisala RS 80A on 12th March 2001 at 12UTC over Lindenberg, Germany

humidity wrt water is, that in regions with a temperature lower than 0 °C, the watervapor saturation pressure with respect to (wrt) ice is lower than wrt water (figure 3.2). It follows, that in supercooled region it is more common, that in case of supersaturation ice crystals are directly formed out of the vapor phase (heterogeneous freezing). To force a freezing event over the liquid phase (homogeneous freezing), we need a much higher relative humidity and also some additional specific properties. - In Figure 3.3 we can see a typical profile of the RHi over Lindenberg, containing a single layer ISSR with max RHi ≈ 130 , obtained from a routine ascent of Vaisala RS 80A on 12th March 2001 at 12UTC. From the data some information

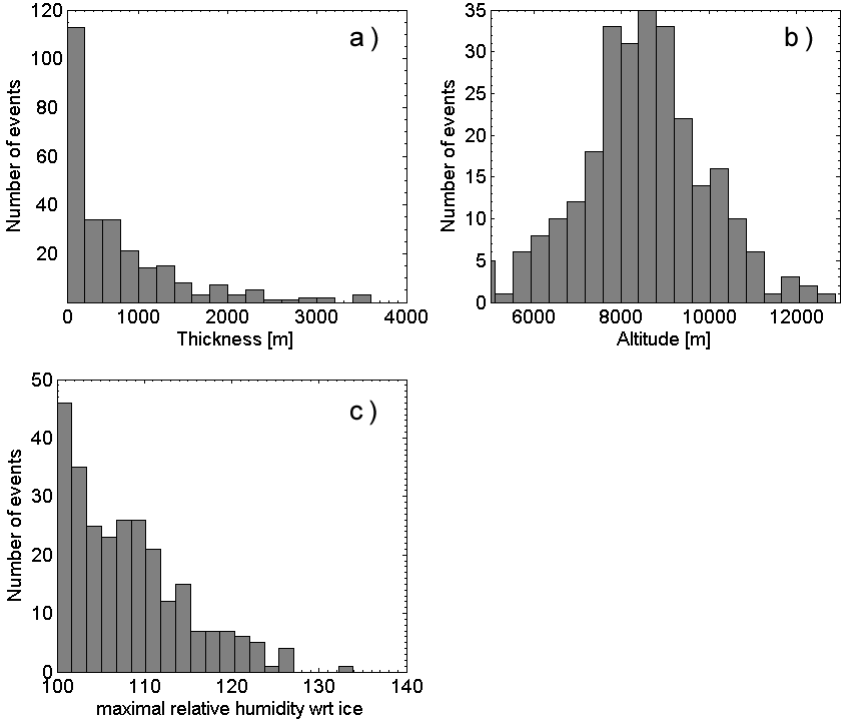


Figure 3.4: Frequency distribution of a) thickness, b) mean altitude and c) maximum RHi, obtained from routine ascent of Vaisala RS 80A over Lindenberg, Germany

on the shape of ISSRs could be obtained: Figures 3.4 a), 3.4 b) and 3.4 c) show frequency distributions of thickness (mean: ≈ 500 m), mean altitude (mean: ≈ 8200 m) and maximum RHi (mean: $\approx 108\%$ RHi), respectively, measured by the radiosondes. The obtained arithmetic mean values of the

mean altitude will be important for the shape of the idealized profiles, used in the next chapter. Although this sort of statistics was carried out extensively in Spichtinger et al. (2003a). By comparing the frequency distribution of the maximum RH_i values with measurements obtained from other measurement techniques (e.g. Ovarlez et al., 2002; Comstock et al., 2004) it is obvious that the radiosondes underestimate the amount of supersaturation. Out of this other studies follows, that a maximum RH_i of more than 160% is not uncommon.

3.3 Radiation Model

For determining the optical properties of a whole atmospheric profile, a radiation transfer model is used. Since the shape of our profiles does not have any horizontal extension, the used model only needs a vertical dimension (single column model, SCM). The radiation code used in the first part of this thesis is the radiative transfer code of the Canadian Center for Climate Modeling and Analysis (CCCma), used as a single column version. For my calculations I only regard the radiation part of the model, i.e. the model runs for only one time step without any dynamics or micro physics. The radiation code is based on a two-stream approximation using four bands in the solar regime (Table 3.1) and nine bands in the thermal infrared (Table 3.2). Out of the nine longwave bands, twelve absorption intervals for the specific trace gases are defined (Table 3.3).

Band No.	Spectral region (μm)
1	0.25 - 0.69
2	0.69 - 1.19
3	1.19 - 2.38
4	2.38 - 4.0

Table 3.1: Wavelengths of the optical bands of the CCCma radiation code - Solar regime

Band No.	Spectral region (μm) / (cm^{-1})
1	3.5 - 5.3 / 1880 - 2820
2	5.3 - 6.9 / 1450 - 1880
3	6.9 - 8 / 1250 - 1450
4	8 - 9 / 1110 - 1250
5	9 - 10.3 / 970 - 1110
6	10.3 - 12.5 / 800 - 970
7	12.5 - 20 / 500 - 800
8	20 - 28.6 / 350 - 500
9	28.6 - ∞ / 0 - 350

Table 3.2: Wavelengths and wavenumbers of optical bands of the CCCma radiation code - Longwave regime

If we want to determine the optical properties of profiles, that are contaminated with cirrus clouds, we first have to describe the optical parameters

Interval No.	Longwave Band No.	Interval strength
1 H_2O	2 + 9	2630.
2 H_2O	7	8.39
3 H_2O	4 + 6	0.219
4 H_2O	5	0.0293
5 H_2O	8	245
6 H_2O	1 + 3	23.5
7 CO_2	7	415
8 CO_2	4 + 5 + 6	0.0127
9 CH_4	4 + 6	n.a.
10 CH_4	1 + 3	n.a.
11 N_2O	4 + 6	n.a.
12 N_2O	1 + 3	n.a.

Table 3.3: Spectral absorption intervals of the CCCma radiation code - Longwave regime. The according longwave bands are listed in table 3.2.

of the ice particles. The required optical ice parameters are the volume extinction coefficient, the single-scattering albedo, and the asymmetry factor. They are parameterized as a function of the ice crystal effective radius and the ice water content following Slingo (1989), Dobbie et al. (1999) and Fu (1996). For the prescribed values of ice water content I use a “reference value” from a fit to several measurements by Schumann (2002, eq. 3.3):

$$IWC_{ref} = \exp(6.97 + 0.103 \cdot T(^{\circ}C)) \quad (3.3)$$

I assume that the ice crystal size is lognormally distributed, i.e.

$$f(L) = \frac{N}{\sqrt{2\pi} \cdot \log \sigma_L} \cdot \exp\left(-\frac{1}{2} \left(\frac{\log\left(\frac{L}{L_m}\right)}{\log \sigma_L}\right)^2\right) \quad (3.4)$$

where N denotes the ice crystal number density. By using the mass-size relation by Heymsfield and Iaquinata (2000) for small columns

$$\left(\frac{m}{m_0}\right) = \alpha \cdot \left(\frac{L}{L_0}\right)^{\beta} \quad (3.5)$$

also the ice crystal mass is lognormally distributed. Here, m_0 and L_0 denote unit mass and length, respectively. I assume a geometrical standard

deviation of $\sigma_L = 1.5$. The calculation of the ice crystal effective radius is based on the following equation (Ebert and Curry, 1992):

$$r_{eff} = \frac{\int_0^{\infty} \left(\frac{A}{4\pi}\right)^{3/2} \cdot f(L) dL}{\int_0^{\infty} \frac{A}{4\pi} \cdot f(L) dL} \quad (3.6)$$

where A denotes the total surface of a hexagonal cylinder. Peter Spichtinger developed a way, to approximate this integral using the moments of the ice crystal mass distribution as described in the Appendix A. The SCM uses the observed temperature, specific humidity and the derived ice water content and effective radius as input and assumes that the cloud fully occupies a layer, i.e. the fractional cloud cover in my simulations is 1. For atmospheric trace gases and for the surface albedo (17%), reference values from the ARM site in Oklahoma are used (Zhang et al., 2005). A solar zenith angle of 60° at a geographical latitude of 52°N for Lindenberg (Germany) is used.

To determine the impact of ISSRs and thin cirrus clouds on remote sensing applications, we have to calculate the changes in the radiation flux for every single band separately. Due to specific technical properties of the CCCma radiation code, it would be afflicted with a lot of work, to extract the output of every single band in the longwave regime. That's the reason why I used another radiation code for this task. This second radiation code, designed by Qiang Fu 1998 (Fu et al. (1998)), is quit similar to the one of the CCCma but more complex. That means, that it also needs more computation time to determine the radiative properties of an atmospheric profile. That's one of the reasons, why the second radiation code is only used for some specific cases. After some changes in the source code of the model, it is possible to determine the radiative fluxes for every single band, according to six bands in the solar regime and twelve bands in the longwave regime (tables 3.4 and 3.5). More about this will be shown in the results section.

Band No.	Spectral region (μm)
1	0.2 - 0.7
2	0.7 - 1.3
3	1.3 - 1.9
4	1.9 - 2.5
5	2.5 - 3.5
6	3.5 - 4.0

Table 3.4: Wavelengths of the optical bands of the radiation code designed by Q. Fu 1998 - Solar regime

Band No.	Spectral region (μm) / (cm^{-1})
1	4.5 - 5.3 / 1900 - 2200
2	5.3 - 5.9 / 1700 - 1900
3	5.9 - 7.1 / 1400 - 1700
4	7.1 - 8.0 / 1250 - 1400
5	8.0 - 9.0 / 1100 - 1250
6	9.0 - 10.2 / 980 - 1100
7	10.2 - 12.5 / 800 - 980
8	12.5 - 14.9 / 670 - 800
9	14.9 - 18.5 / 540 - 670
10	18.5 - 25.0 / 400 - 540
11	25.0 - 35.7 / 280 - 400
12	35.7 - ∞ / 0 - 280

Table 3.5: Wavelengths and wavenumbers of the optical bands of the radiation code designed by Q. Fu 1998 - Longwave regime

Chapter 4

Results and Discussion

4.1 Radiosonde Profiles

For this part of the investigation I assume that all ice supersaturated layers found in the radiosonde data are cloud free. However, I have no evidence from the measurements, because of lack of detection techniques for ice crystals on board of the radiosonde (see also Spichtinger et al., 2003a), but for estimation of the impact of real ISSRs this is a justified assumptions.

As described in section 3.2, 293 of the 1563 vertical profiles measured over Lindenberg (Germany) contain a single layer ISSR. The following procedures are only done to these qualified 293 vertical profiles, after they have been interpolated and processed as described. We now obtain heating rates (longwave & shortwave) for the vertical profile and for top of the atmosphere (TOA) fluxes of the outgoing longwave radiation (OLR) and net shortwave radiation. Additionally, the radiation transfer was calculated for the saturated profile, i.e. in the supersaturated layer the values were set to $RHi = 100\%$. To get a better overview, how much an ISSR influences the radiative transfer, I define the ISSR Radiative Effect (IRE) (equation 4.1) as a function of the heating rates. It is defined as the difference between the maximum and the minimum value of the difference between the heating rates of the supersaturated ($HR(ISSR)$) and the saturated case ($HR(sat)$). This is a lower bound for the radiation impact of ISSRs because of the underestimation of ice supersaturation in spite of the correction.

$$IRE = \max [HR(ISSR) - HR(sat)] - \min [HR(ISSR) - HR(sat)] \quad (4.1)$$

A typical RHi profile of a radiosonde ascent over Lindenberg is shown in figure 4.1, here we obtain a maximal value of the RHi of about 130% at

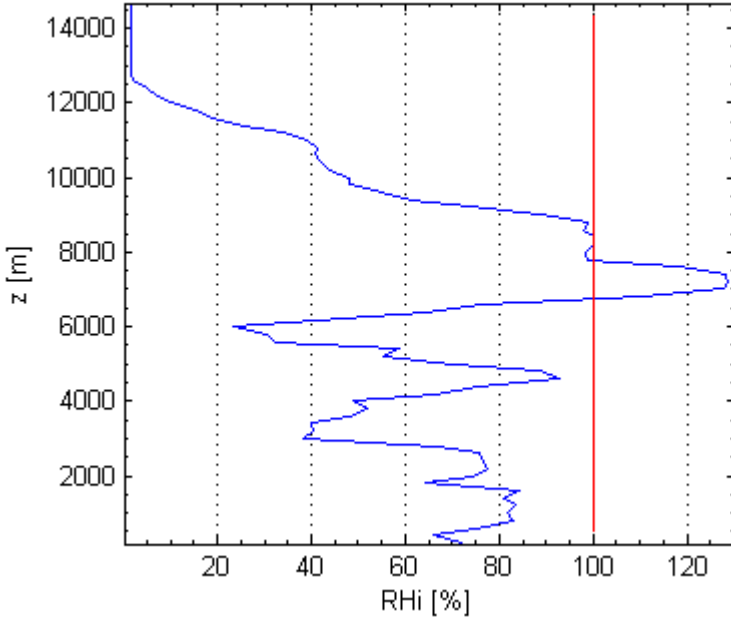


Figure 4.1: Relative humidity wrt ice profile, containing a single layer ISSR with max $\text{RH}_i \approx 130$, obtained from routine ascent of Vaisala RS 80A on 12th March 2001 at 12UTC over Lindenberg, Germany

an altitude between 7500 m and 8000 m. On the basis of this example, I want to explain, what happens with the radiation passing through a layer with different RH_i peak values. In principle, there is almost no effect on the incoming solar radiation due to the ISSR, only the outgoing longwave radiation (emitted by earths surface) is affected by absorption due to the (enhanced) water vapor within the layer. For the longwave radiation there is a strong warming in the lower part of the layer with enhanced water vapor due to the absorption of the radiation from the surface. In the upper part of the supersaturation layer there is a cooling; this means that the water vapor molecules emit radiation into space.

The difference between the heating rates of the saturated and the supersaturated case (Figure 4.2) is, that at the lower boundary, the supersaturated case absorbs more longwave radiation and therefore its heating rate values are larger. At the upper boundary, we observe the opposite case, because the supersaturated layer emits more radiation than the saturated one, due to the higher amount of water vapor. Also shown in this figure is the ISSR

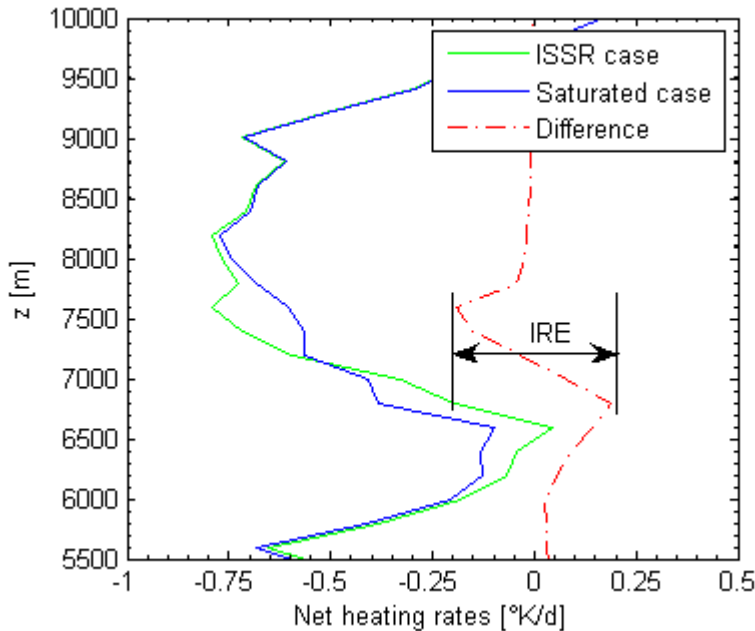


Figure 4.2: Net heating rates obtained from the radiosonde ascent on 12th March 2001 at 12UTC over Lindenberg Germany, calculated with the radiation transfer model from the SCM CCCma

radiative effect (IRE), as a function of the difference between the heating rates of the saturated and the supersaturated profile. In this case, the value of the IRE is about 0.4. This basic impact, induced by the enhanced water vapor amount, can be observed in every processed ISSR-profile used for this thesis.

Just after the analysis of the first few profiles, it becomes obvious, that the ISSR impact on radiation depends a lot on the shape of the RH_i profile. The maximum value of the supersaturation depends strongly on the thickness of the supersaturation. This can be seen in Figure 4.3. Also the RH_i gradient at the lower and upper boundary of the ISSR is important for the strength of the IRE. Because of the variability of every parameter in the measured radiosonde profile, it is hard to use them for my sensitivity studies. For this purpose, idealized profiles are much more useful.

By investigation of all 293 vertical profiles, it can be seen that the ISSR Radiative Effect IRE correlates very well with the maximal RH_i (correlation coefficient: $r=0.91$). Additionally, it can be seen that high values of RH_i oc-

cur mainly in thicker ISSRs (Figure 4.3). For my purposes, the IRE is very

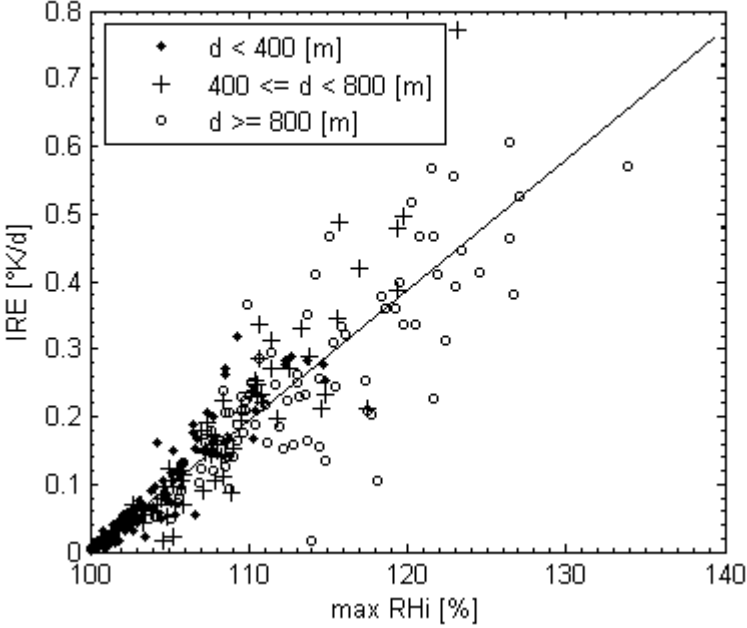


Figure 4.3: ISSR radiative effect IRE of 293 single layer ISSRs, obtained from routine ascent of Vaisala RS 80A over Lindenberg Germany, calculated with the radiation transfer model from the SCM CCCma

suitable, because it depends neither on the mean altitude nor on the temperature (which is one of the main changing parameter during a daily cycle) of the corresponding layer. It mostly depends on the main characteristics of an ISSR, the relative humidity and the thickness of the supersaturated layer. Therefore, profiles which had been recorded during the night can be handled the same way as the day-profiles. The sensitivity on the shape and the specific gradient of the RHi profile (at the lower and upper ISSR boundary) will be discussed later in this thesis (Section 4.2), using idealized RHi profiles embedded inside a standardized atmosphere (derived out of the properties of the processed 293 single layer ISSR profiles).

4.2 Idealized ISSR Profiles and its impact on radiation

In order to obtain an average information of the radiative properties of ISSRs, a couple of idealized profiles are defined. First of all, mean profiles for the variables temperature and pressure are calculated out of the 293 qualified single layer ISSR profiles. The tropopause is located at $z_{TP} \sim 12000$ m, and defined with a non-dynamical formulation. That means, that above this border, the vertical temperature gradient becomes positive. The mean profile for the relative humidity is constructed in a more sophisticated way: The altitude and thickness for the ISSR were determined by the average values presented in section 3.2 and in Figure 3.4. The center of all idealized ISSRs used in the following section is located at $z_c \approx 8200$ m and their thickness will always be 1200 m (This is more than the mean value of 500m, because the coarse model resolution).

Parameter	Value
Altitude	8200 [m]
Thickness	1200 [m]
Temperature	as described in Figure 4.4 a)
pressure	as described in Figure 4.4 b)
max RH _i	varies: 60% - 130%
upper RH _i	varies: 5% - 60%
lower RH _i	60%

Table 4.1: Different parameters of the idealized ISSR profiles

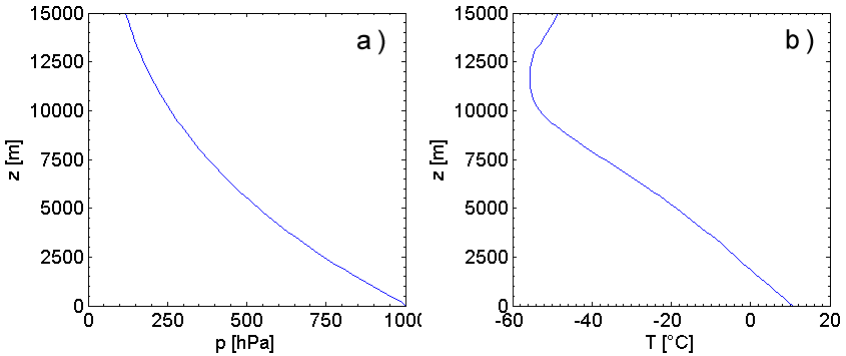


Figure 4.4: Idealized profiles for: a) pressure [hPa], b) temperature [°C]

The shape of the RH_i profiles is built using two different assumptions (Figure 4.5). First, I define that inside the supersaturated layer the maximum RH_i value is constant. The RH_i of the ISSR now looks like a rectangular bar. This most idealized shape is used in most of the sensitivity studies and will be flagged as an "rectangular" ISSR. In a second approximation, the shape of the RH_i inside of the ISSR is formed more detailed, referring to the shape of the measured RH_i profiles. For this case I assume, that the maximum RH_i peak is only formed out of one single point. By changing the shape of the RH_i peak, we modify important parameters like the total amount of watervapor inside the supersaturated layer, or the RH_i gradient at the top of the ISSR. - The RH_i in the region above the ISSR (named as "upper RH_i" (uRH_i)) is also variable, because by changing this value, we will also change the RH_i gradient at the upper ISSR boundary. Above the tropopause, the RH_i has a constant value of 5%. This modulations will have an impact on the radiative transfer and also on the radiative absorption and emission at the boundaries of the ISSR.

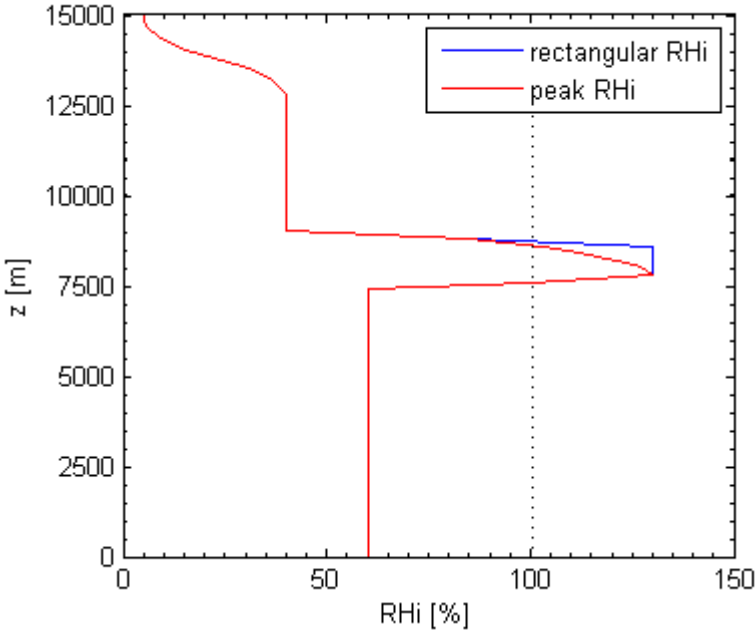


Figure 4.5: Idealized RH_i profiles with rectangular- and peak-shape

First, I will use idealized profiles with a rectangular RH_i shape (as shown in Figure 4.5) and vary the maximal value of the RH_i within the ISSR. The up-

per RHi is hold constant at 40%. This will give us a first overview about the sensitivity of the local heating rates and the radiative flux at the top of the atmosphere (TOA). The changes in the heating rates are shown in Figure 4.6, where the maximum relative humidity is changed between the values 80%, 100% and 130%. Note that although a value of $RHi = 130\%$ seems to be quite high, several other measurements suggest that also in the mid latitudes values up to $RHi = 160 - 170\%$ might be possible (see e.g. Ovarlez et al., 2002). Hence, this is a lower bound of possible radiative impacts of ISSRs. For the reference case (i.e. saturated profile) the difference between the heating and the cooling peak is about $0.83 K/d$, in the supersaturated case the difference increases to a value of $1.24 K/d$ (i.e. about 1.5 times larger than for the reference case), whereas in the subsaturated case the difference is reduced to $0.42 K/d$ (i.e. almost half of the value of the reference case). These values can be translated into the IRE, i.e. for the supersaturated case we find heating rates leading to a value of $IRE = 0.56 K/d$ whereas for the subsaturated case the heating rates reduce to $IRE = -0.41 K/d$. In Figure

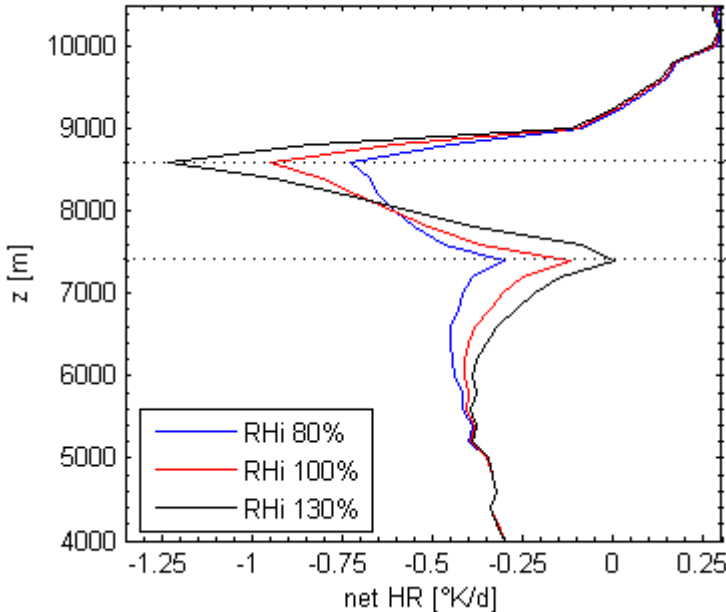


Figure 4.6: Net heating rates of three idealized atmospheric profiles (rectangular shape), with different maximum RHi values inside an ISSR, $uRHi = 40\%$

4.7 a) we can see the IRE as a function of the maximum RHi (two more RHi profiles are added, the first with 60% max. RHi and the second with 108% max. RHi (this profile stands for the mean max. RHi value out of the 293 measured single layer profiles)). Furthermore, Figure 4.7 b) shows the outgoing longwave radiation (OLR) as a function of the max. RHi. We find a noticeable effect on the outgoing longwave radiation at the top of the atmosphere (TOA): By varying the maximal RHi in the (super-) saturated layer from 60% to 130%, the OLR varies by about 1 Wm^{-2} . Additionally, it can be observed, that the ISSRs only have a negligible effect on the surface radiation budget (also called "ground effect").

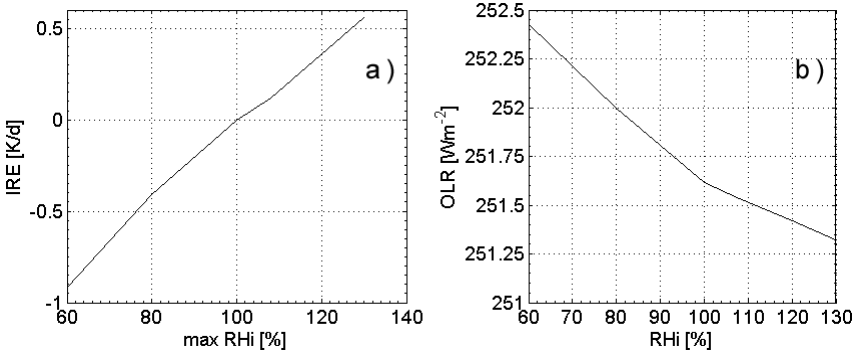


Figure 4.7: a) ISSR radiative effect IRE as a function of the max RHi, b) Outgoing longwave radiation OLR as a function of the max RHi. Obtained out of idealized profiles (rectangular shape), uRHi = 40%

As said before, the water vapor gradient at the upper boundary of the ISSR may influence the local heating rates by changing the amount of emitted longwave radiation. To get a better overview, three different cases with changing relative humidities above the ISSR are determined with the radiation transfer model. As it is shown in Figure 4.8 b), increased RHi gradients lead to a higher amount of cooling at the upper boundary of the ISSR. After this differences, the curves approach each other again, although the amount of water vapor of the three profiles is diverging.

This fact shows us, that the heating rates of an ISSR might be mainly a function of the vertical gradient of the water-vapor amount. Therefore, we define the function 4.2 for the change of the heating rates dHR in dependence of the water-vapor gradient dq_v .

$$dHR = \frac{\Delta HR}{\Delta z} \parallel dq_v = \frac{\Delta q_v}{\Delta z}$$
$$dHR = f(dq_v) \tag{4.2}$$

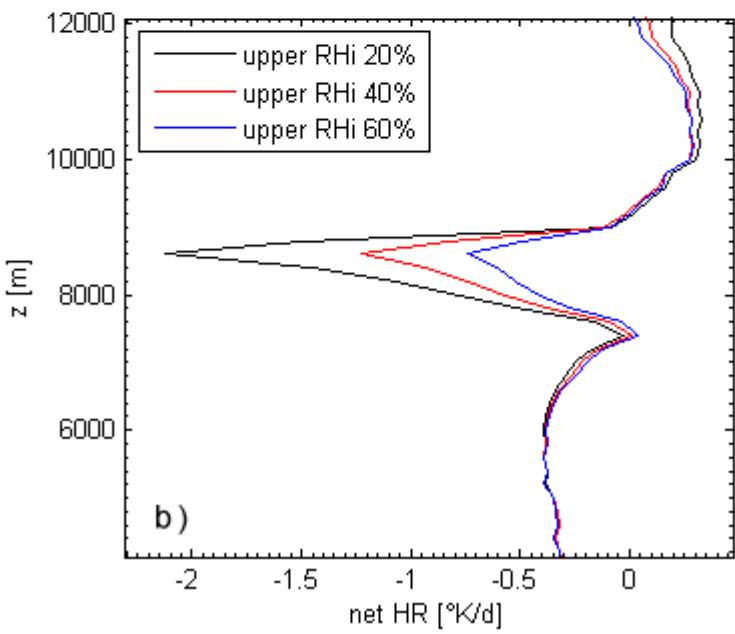
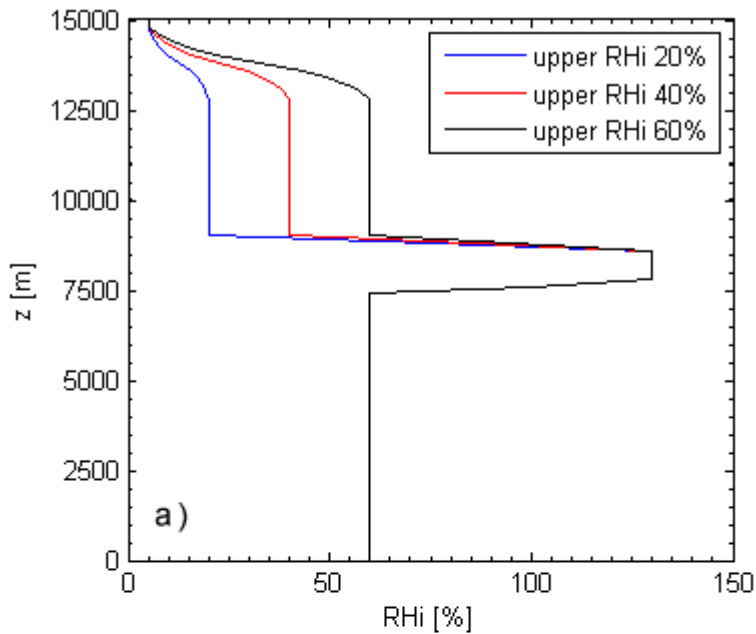


Figure 4.8: a) three different idealized profiles (rectangular) with variable upper RHi values, b) and their heating rates

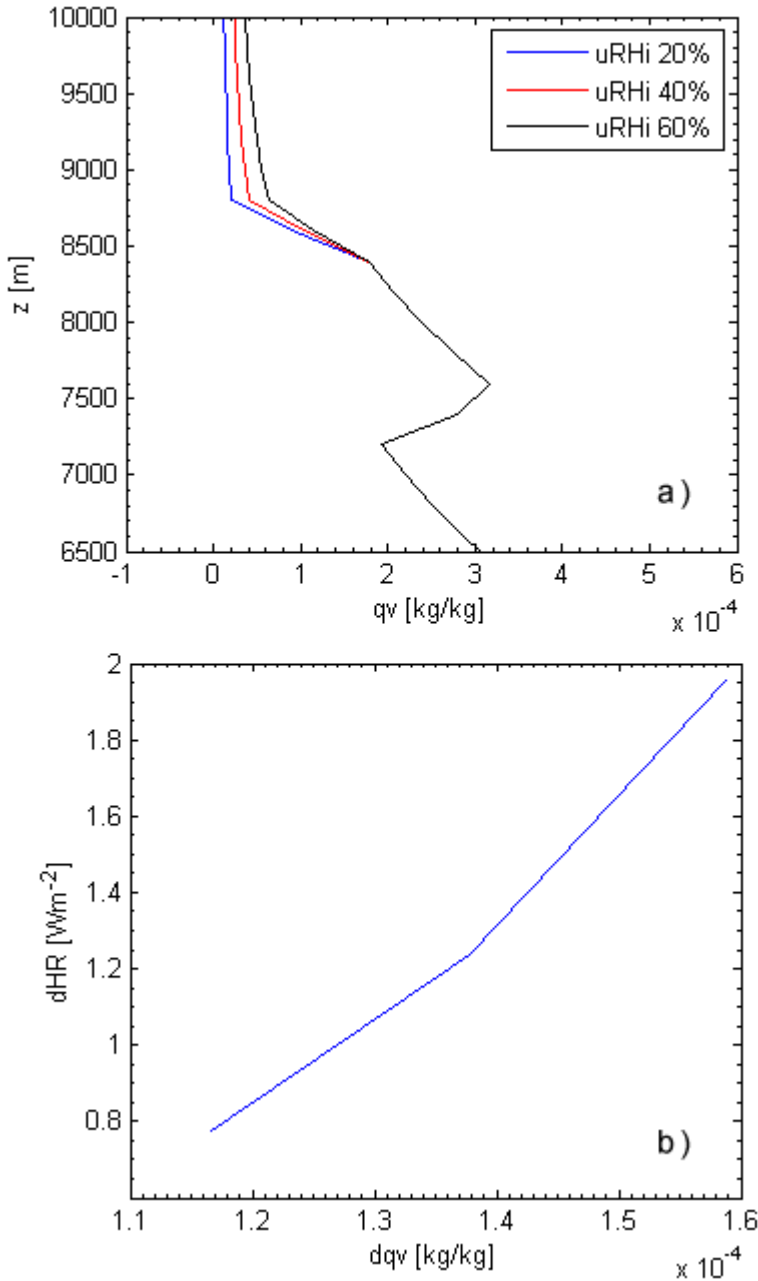


Figure 4.9: a) three different idealized profiles (rectangular) with variable upper water vapor amount, b) and the change in their heating rates

The different water vapor amount and the heating rates according to function 4.2 are shown in Figure 4.9. It becomes obvious, that the basic approach which has been done at the beginning of this chapter seems to be true. It has to be considered that the sensitivity of the local heating rates not only has to be a function of the vertical gradient of the water vapor and its maximum value. Other factors like the temperature, the altitude or the distribution of important trace gases may also modulate the radiative transfer inside ISSRs. However, I don't have the time to take this other modulators into account. This may be a possible topic for future work.

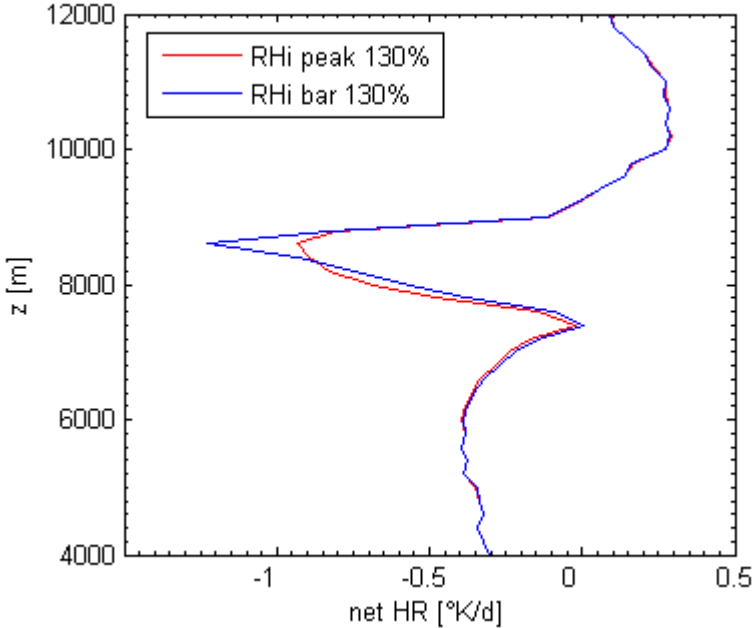


Figure 4.10: different heating rates of a rectangular and a peak ISSR, RHi 130%, uRHi 40%

After investigating the impact of most idealized ISSR profiles (rectangular), I want to look at profiles with a more realistic shape (peak-shape in Figure 4.5). The mean difference between the rectangular- and the peak-shape is located at the upper region of the ISSR, whereas the shape at the lower region is quite the same. The peak-shape ISSR has less water vapor in its upper region, and also a lower vertical water vapor gradient. This leads to a much smoother heating-rates peak at the upper boundary with a decreased cooling-effect (Figure 4.10). This kind of peak is much more realistic, but for sensitivity studies, the smooth heating-rates peak is not suitable. The investigation of the impact of "peak-profiles" with different maximum RHi values showed, that for relative humidities bigger than 100%, the cooling at the upper ISSR boundary propagates to a constant value. The reason for that is a very low change of the vertical water vapor gradient for this kind of profiles.

4.3 Radiative Impact on Local ISSR Dynamics

The main reason, why sensitivity studies on local heating rates are done, is that specific temperature changes inside ISSRs can influence strongly the local dynamics. As a possible consequence, a cirrus cloud could form due to a radiative induced convection. Convection is best explained by the so-called lifted parcel theory. Here, the environment of the parcel is not affected by this displacement, and the upward force affecting such a rising plume (i.e. parcel) of air is buoyancy, which is defined by:

$$B = -\frac{\rho_p - \rho_e}{\rho_e} \cdot g = \frac{T_v(z)_p - T_v(z)_e}{T_v(z)_e} \cdot g \quad (4.3)$$

The difference in density (left term) or in virtual temperature (right term) between the rising parcel (p) and the parcel environment (e) causes the updraft. Consequently, a parcel with greater temperature and less density will be controlled by buoyancy and displaced vertically. To describe the stability of an atmospheric stratification, we use a standard criterion for the stability of the atmosphere, using the potential temperature θ as defined:

$$\theta(z) = T(z) \left(\frac{p_0}{p(z)} \right)^\kappa, \quad \kappa = \frac{R}{c_p} \quad (4.4)$$

where p_0 is the ground pressure and z the local altitude. By differentiating the adiabatic-equation by the vertical coordinate z , we get following three criterion for the stability of the atmospheric stratification:

$$\begin{aligned} \frac{\partial \theta}{\partial z} &> 0 && \textit{stable stratification} \\ \frac{\partial \theta}{\partial z} &= 0 && \textit{neutral stratification} \\ \frac{\partial \theta}{\partial z} &< 0 && \textit{unstable stratification} \end{aligned}$$

As we can see, a stratification becomes unstable, when the vertical gradient of the potential temperature is lower than zero. For this purpose, the radiative transfer model has been embedded in a new program environment, which can evaluate the change of the potential temperature for some time steps by adding the heating rates of each increment. An idealized ISSR with a maximum RHi of 130% and a weak-stable stratification has been constructed and then been exposed to constant longwave radiation. I only use longwave radiation because I want to simulate a night scenario with no

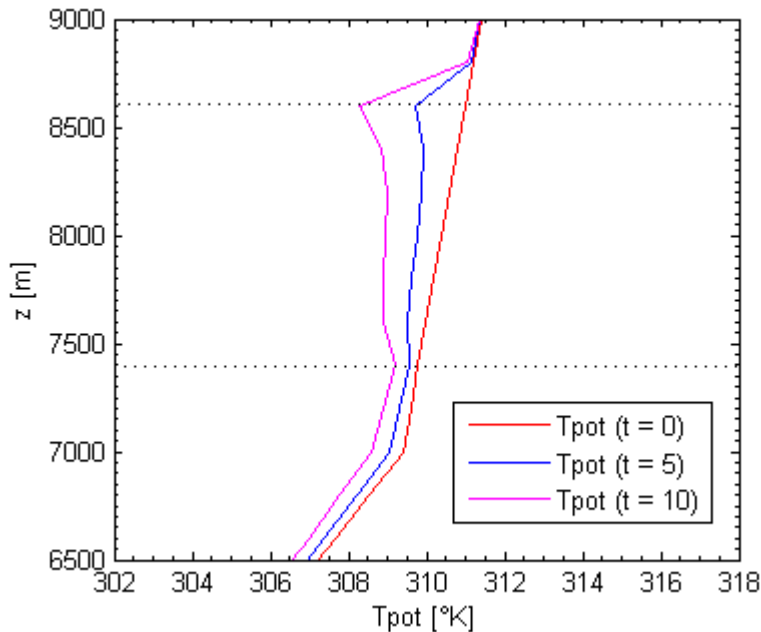


Figure 4.11: Potential temperature of an ISSR (between the dashed lines) and its change due to the impact of longwave radiation

sunlight (shortwave) and its afflicted intensity change during the day. This is much easier to investigate than a scenario with changing conditions. As we can see in Figure 4.11, the stratification of the ISSR starts to destabilise after the first 5 hours at its lower boundary and also at its upper boundary. After the next 5 hours, we can observe a strong destabilisation at both boundaries of the ISSR. Again, the impact on radiation and the consequent change of the temperature is based on two different processes: the absorbing of longwave radiation at the lower boundary, and the emission of longwave radiation at the upper boundary of the ISSR.

The stability of the stratification is shown in Figure 4.12, where the vertical gradient of the potential temperature has been plotted after the profile has been exposed 10 hours to longwave radiation. The unstable stratification is obvious. How this destabilisation of the stratification exactly influences the evolution of the ISSR can not clearly be examined now. Maybe, a cirrus cloud could form due to the convection and an induced nucleation of cloud ice. To answer this question more precisely, a better model has to be used, which includes a dynamic part and also a code for the ice-physics. For

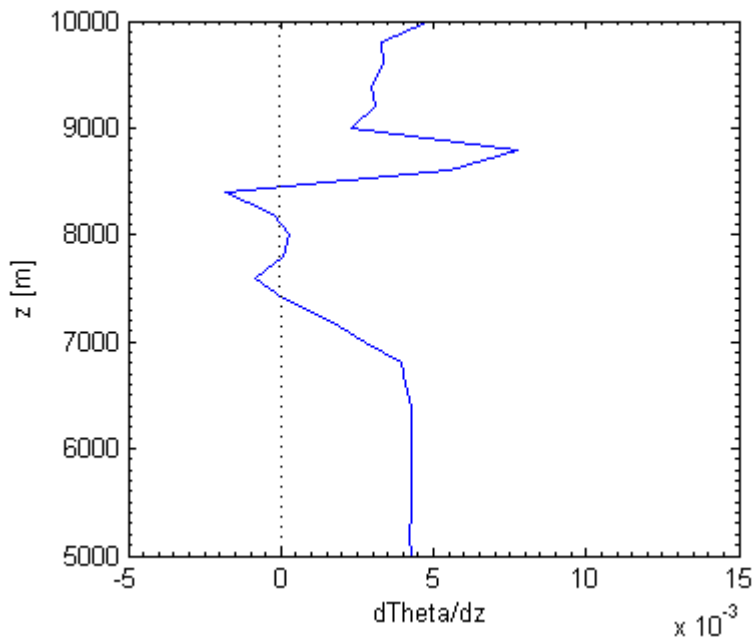


Figure 4.12: The vertical gradient of the potential temperature, unstable stratification if it is below zero

for this purpose, I try to implement a radiation code inside the cloud resolving model EULAG. This task has not been finished yet, and will not be a part of this thesis. This small sensitivity analysis on the dynamics should only be a short outlook on future investigations.

4.4 Thin Cirrus Clouds and its Impact on Radiation

Now cloud ice is included into the supersaturated layer in order to determine the impact of thin cirrus clouds (with ice supersaturation inside). The amount of cloud ice is not big, because only thin cirrus clouds have to be formed. Thin cirrus clouds are hard to detect, hence they can be a source of errors for remote sensing applications (e.g. for the detection of aerosol optical depths, discussed in the next section).

Although we now include ice crystals into our vertical profile we do not set $RHi = 100\%$ inside the cloud. The maximum RHi of 130% is still hold, because there is evidence from measurements, that (moderate) ice supersaturations are frequently found inside (thin) cirrus clouds (see e.g. Ovarlez et al., 2002; Spichtinger et al., 2004; Peter et al., 2006). In a next step, the ice

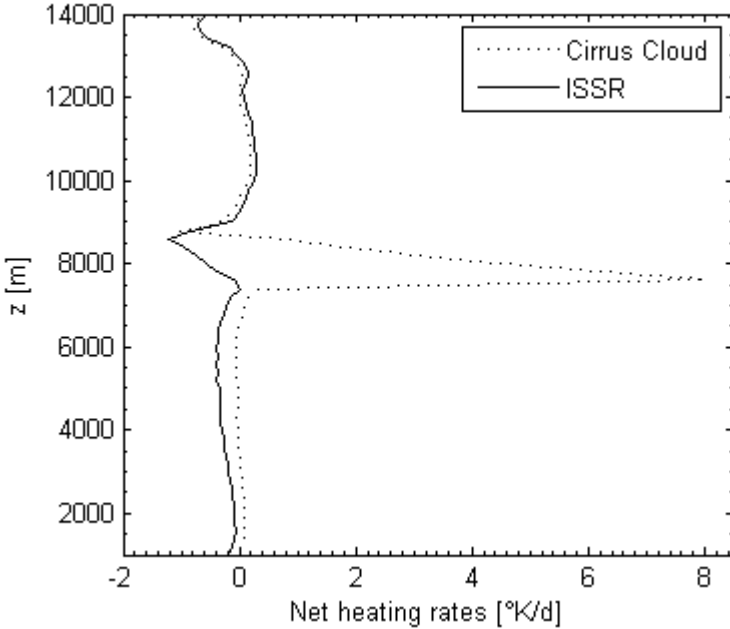


Figure 4.13: Net heating rates of a ISSR and a thin cirrus cloud (50% IWC_{ref} , $N = 1000 \text{ L}^{-1}$, optical depth $\tau = 0.84$, max RHi 130% (rectangular))

water content (IWC) and the ice crystal number density, two important parameters of the microphysical structure of the cirrus cloud, are varied. The

values for IWC range between 1% and 100% of the reference value given by equation 3.3. Implicitly, I also consider a change in altitude because of the temperature dependence of the reference value. The ice crystal number density N varies between 20 and 1000 crystals per liter; this is a range well known from measurements in the mid latitudes (e.g. Quante, 2004). From both variables the effective radius r_{eff} can be calculated using equation 3.6. The full derivation is found in the Appendix A.

Figure 4.13 shows the differences in the net heating rates between a cloud free ice supersaturated layer and the same layer including a cirrus cloud: Whereas for the cloud free ISSR only the longwave radiation is absorbed by the enhanced water vapor within the layer, in case of a cloudy layer the ice crystals additionally absorb energy in both frequency bands (longwave and shortwave) and the incoming solar radiation is partly reflected. Hence, the heating effect within the cloudy layer is much higher than in the clear air case (with differences up to +8 K/d at the lower boundary of the cloud/ISSR). In the case of cirrus clouds a non-negligible effect on the surface radiation budget can be observed. At the top of the atmosphere the radiative flux changes in a noticeable amount. Because of increasing values of IWC and ice particles number density the cloud optical depth and albedo are increasing too. More radiation is absorbed at the bottom of the cloud (warming), and also more solar radiation is reflected at the top of the cloud (cooling). Figures 4.14 - 4.15 show the changes of the optical depth and the fluxes as a function of the IWC and the ice particle number density.

The optical depth depends strongly on both, cloud ice and ice crystal number density. For a given ice water content, the optical depth weakly increases for increasing number concentration, i.e. for decreasing effective radius due to stronger scattering at small crystals (Figure 4.14 a)). This is the main feature, which triggers also the properties of outgoing longwave radiation (Figure 4.14 b)) and reflected shortwave radiation (Figure 4.15 a)). Due to the more efficient absorption of longwave radiation emitted from the surface in the cirrus layer, the OLR decreases with increasing ice crystal number density at constant IWC values. By using Figure 4.14 a) this means that the OLR decreases with increasing optical depth. For the reflected shortwave radiation it is the other way round: The reflected shortwave radiation increases with increasing optical depth. The question arises which of these two effects is dominant for different values of IWC and ice crystal number density, i.e. in which regimes a net warming or cooling can be observed. For this purpose we investigate the total outgoing radiation: The total outgoing radiation is defined as the sum of the outgoing longwave radiation and the reflected shortwave radiation (Figure 4.15 b)). For clouds with less than 320

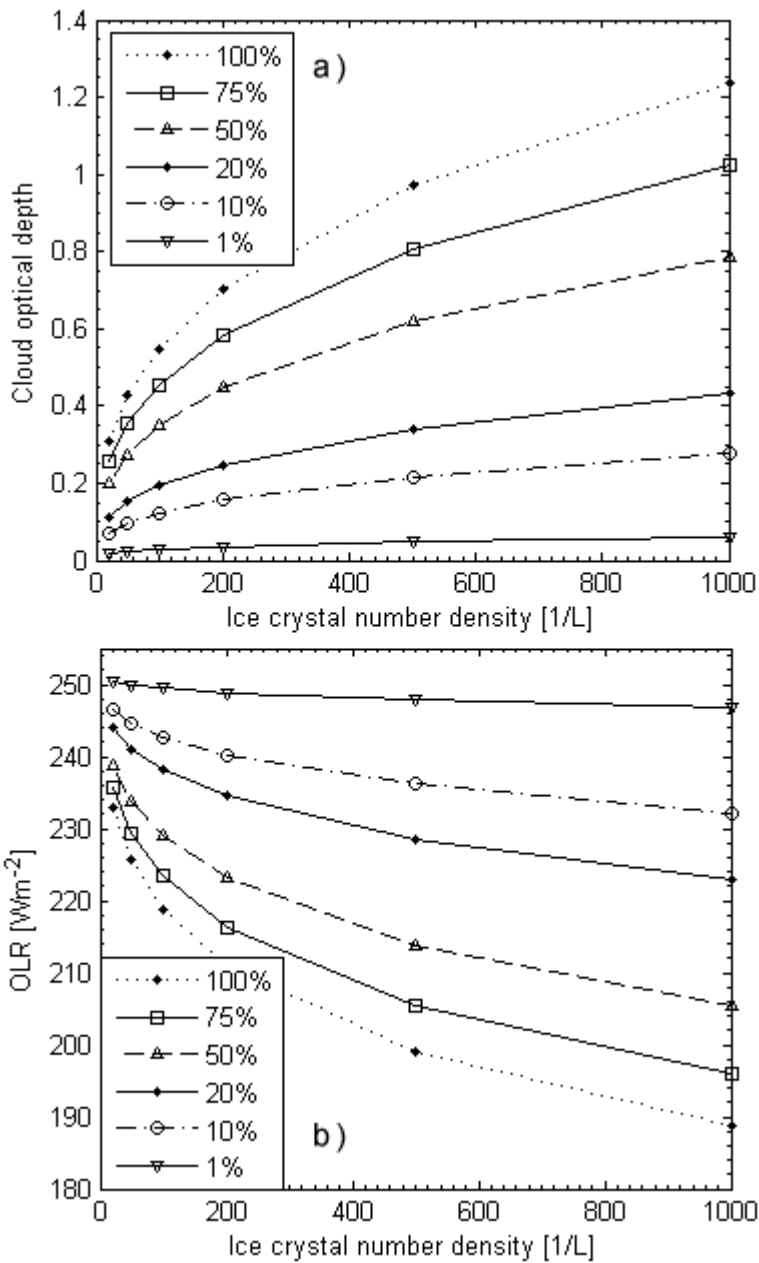


Figure 4.14: a) optical depth and b) outgoing longwave radiation at the top of the atmosphere of the simulated cirrus clouds (thickness = 1200 m) for different values of IWC (the percentages denote % of IWC_{ref} , eq. 3.3) and ice crystal number density (in L^{-1})

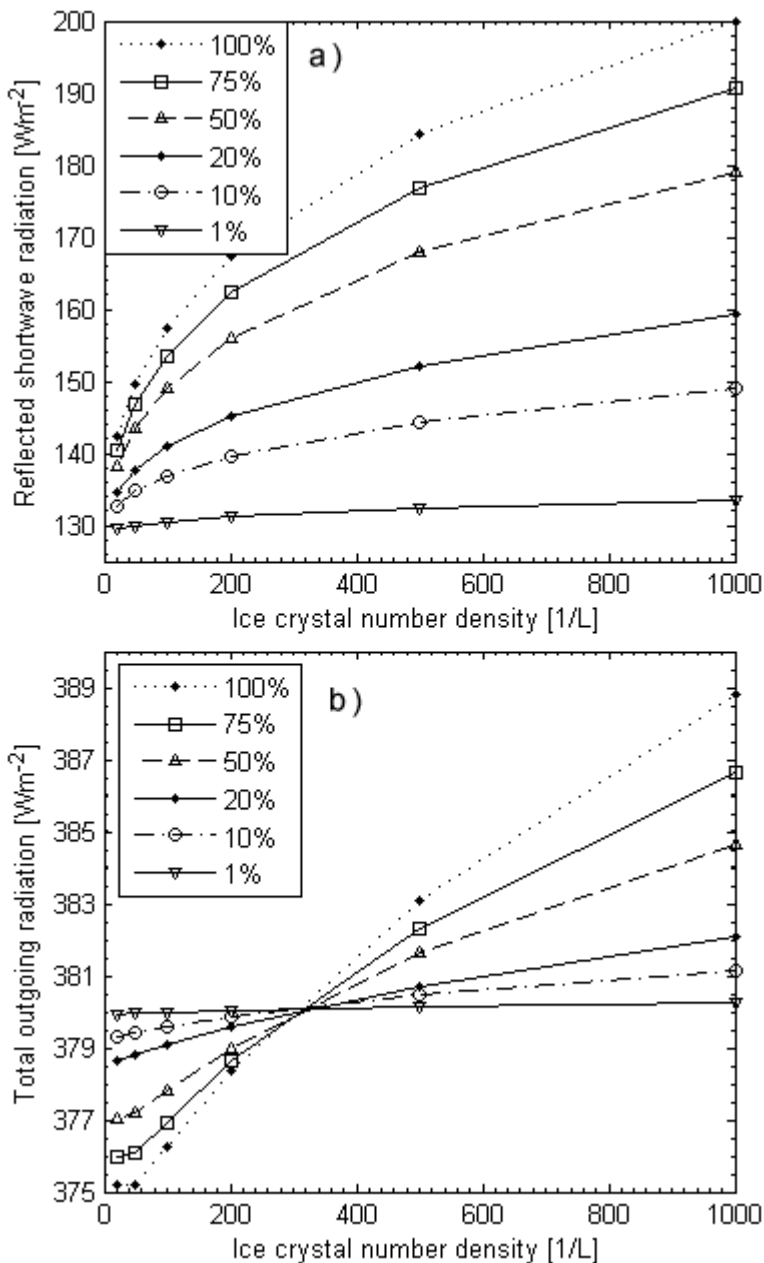


Figure 4.15: a) outgoing shortwave radiation and b) total outgoing radiation at the top of the atmosphere (i.e. sum of OLR and reflected shortwave radiation) of the simulated cirrus clouds (thickness = 1200 m) for different values of IWC (the percentages denote % of IWC_{ref} , eq. 3.3) and ice crystal number density (in L^{-1})

ice crystals per liter the total outgoing radiation is lower than for thicker clouds (increased IWC, larger crystals). The reason for this warming effect is, that the amount of absorbed longwave radiation is larger than the reflected shortwave radiation. For clouds with more than 320 ice crystals per liter the opposite effect is found. Now, the loss of energy by reflecting shortwave radiation dominates the longwave radiation absorption and leads to a general cooling effect. By comparing one particular case of the change

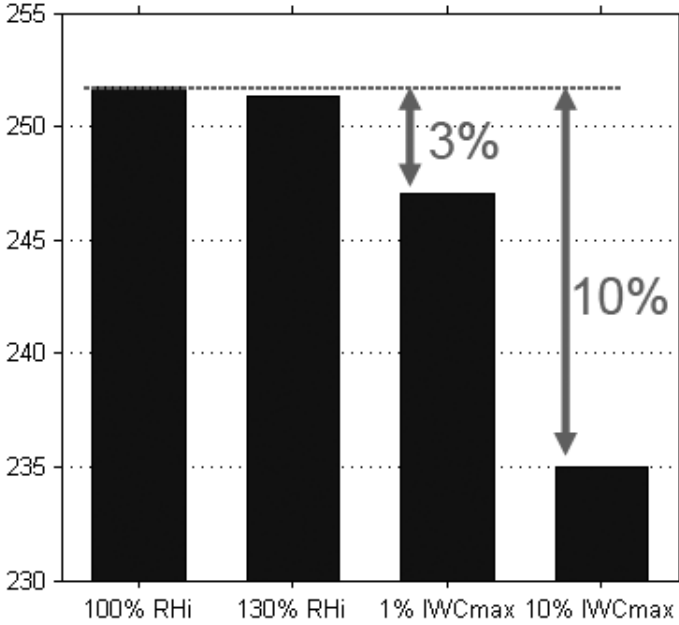


Figure 4.16: Outgoing longwave radiation OLR at TOA for four different cases (both clear sky and cirrus cloud)

in the outgoing longwave radiation OLR at the top of the atmosphere TOA, we can see that also very thin cirrus clouds (with an optical depth τ of ≈ 0.1) can decrease the OLR about 3% (Figure 4.16). This error becomes much bigger for increasing IWC and N (for a cloud with $\tau \approx 0.4$ the error in the OLR is about 10%).

4.5 Impact of incorrectly formed cirrus clouds in GCMs

Although the existence of ice supersaturation in clear air and the formation of ice crystals at high ice supersaturations is known, almost all cloud parameterizations used in large scale general circulation models form cirrus clouds at ice saturation. This leads to differences in the produced cloud ice mixing ratios and to timely shifted occurrences of cirrus clouds, although it is not clear if in nature a cirrus cloud would have been formed. Cloud free ice supersaturation can last for long times and there is no physical reason to form a cirrus cloud from the ice supersaturation as long as the criterion for homogeneous (i.e. really high supersaturations) or heterogeneous nucleation (i.e. enough ice nuclei and reaching the nucleation threshold) are not fulfilled.

By comparing the results of the sections 4.2 and 4.4 we can conclude, that the changes in all properties (i.e. local heating rates vary up to 8 K/d, or the tremendous changes in the TOA flux (both shortwave and longwave)) show that incorrectly formed cirrus clouds can strongly influence the radiative properties. However, it is not possible to estimate this impact for GCMs, because often cloud parameterizations are tuned such that the radiation is balanced at the top of the atmosphere. Hence, an insufficient representation of clouds does not necessarily lead to large inconsistencies in the model.

4.6 The Impact on Remote Sensing

In the sections 4.1 - 4.4 we have seen, that ice supersaturated regions and thin cirrus clouds can influence the local heating rates and also the TOA flux in both shortwave and longwave spectrum. Beneath the not negligible effect on the radiative balance of the atmosphere and its local dynamics, other applications are also afflicted by the potential error in the radiative flux. At this point, I want to try to estimate the potential changes in the radiation received from different sensors, used on board of remote sensing satellites. There would be a lot of different sensors, that would be suitable for this investigation. Two sensors are taken into account, the AVHRR/3 and the IASI.

- The Advanced Very High Resolution Radiometer/3 (AVHRR/3) is a multipurpose imaging instrument used for global monitoring of cloud cover, sea surface temperature, ice, snow and vegetation cover characteristics and is currently flying on NOAA-15 and NOAA-16 (both on a polar orbit with an altitude of $\approx 800\text{km}$). The AVHRR/2 version of the instrument is currently flying on the NOAA/TIROS-N series of spacecraft in a five-channel version (e.g. Eumetsat, ESA). The AVHRR/3 is a six channel scanning radiometer providing three solar channels in the visible-near infrared region and three thermal infrared channels. For our purpose, the channels are very well distributed both in solar and longwave regime (table 4.2, column 1, Figure 4.18, half power points stand for the bands boundaries).
- The Infrared Atmospheric Sounding Interferometer is composed of a Fourier transform spectrometer (IASI) and an associated Integrated Imaging Subsystem (IIS). The Fourier transform spectrometer provides infrared spectra with high resolution between 3.6 to $15.5 \mu\text{m}$ ($645 - 2760 \text{ cm}^{-1}$). The IIS consists of a broad band radiometer with a high spatial resolution. However, the information of IIS is only used for co-registration with the AVHRR. - The main goal of the IASI mission is to provide atmospheric emission spectra to derive temperature and humidity profiles with high vertical resolution and accuracy. Additionally it is used for the determination of trace-gases such as ozone, nitrous oxide, carbon dioxide and methane, as well as land- and sea surface temperature and emissivity and cloud properties. IASI has 8461 spectral samples, aligned in three bands between 15.5 and $3.63 \mu\text{m}$ ($645 - 2760 \text{ cm}^{-1}$), with a spectral resolution of 0.5 cm^{-1} (FWMH) after apodisation (L1C-spectra). The spectral sampling interval is 0.25

cm-1 (e.g. Eumetsat, ESA). - Using the three different bands of IASI (without the high spatial resolution of every spectral sample), we have a nice cover of the longwave radiation regime (table 4.3 column 1, Figure 4.17).

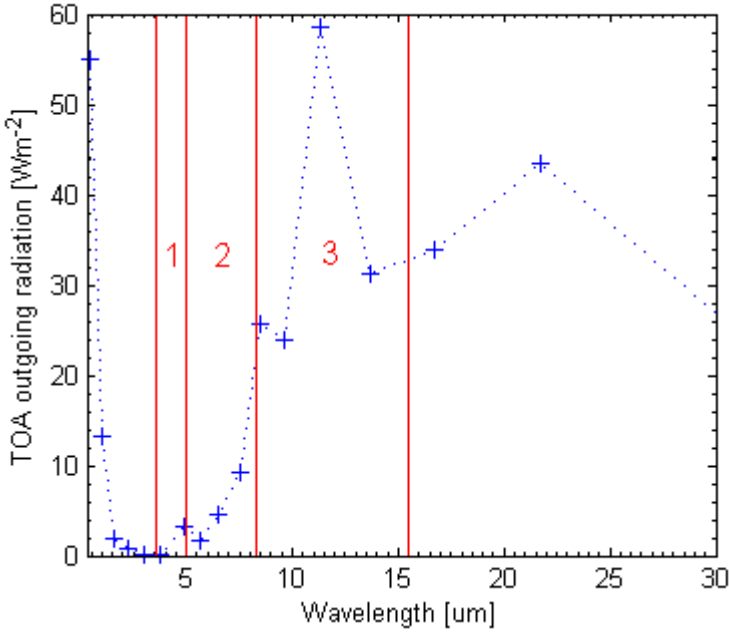


Figure 4.17: The spectral bands of the IASI, blue crosses stand for the total outgoing radiation of each spectral band of the radiation transfer model (in Wm^{-2}), reference case (RHi 100%)

In a next step, the outgoing radiation (TOA) is calculated with the second radiation transfer model (designed by Q. Fu 1998, more at section 3.3). With a spacial resolution of 18 Bands, it is possible to resolve the spectrum of the outgoing shortwave- and longwave-radiation more precisely. Because the outgoing radiation E we get out of the model is already integrated over the width of the model specific bands, we first have to divide through the width of each band to get the spectral radiance L_{λ} . After that, the L_{λ} is again integrated over the specific bands of both sensors (AVHRR/3, IASI):

$$E_i = \int_{\lambda_{1,i}}^{\lambda_{2,i}} L_{\lambda,i} d\lambda \quad (4.5)$$

where the unit for E_i is Wm^{-2} .

To obtain the radiative impact on the different spectral bands of the two sensors, 4 atmospheric profiles are defined (as described in section 4.2). Two profiles are cloud free with maximum RHi of 100% and 130% (ISSR), where the saturated profile will be handled as a reference case. The other two profiles have a thin cirrus cloud within the supersaturated layer (RHi 130%; cirrus1: $N = 100$, $IWC = 0.1mg\ m^{-3}$, $\tau \approx 0.1$; cirrus2: $N = 200$, $IWC = 1mg\ m^{-3}$, $\tau \approx 0.5$).

In table 4.2 the outgoing radiation for the four different cases is shown using the six spectral bands of the AHVRR/3. It is obvious, that the change of the relative humidity from 100% to 130% does not influence the intensity of the received radiation at all. So, the impact of ice supersaturated regions can be neglected using AVHRR/3. The impact of thin cirrus cloud is much stronger and has its maximum for band 3a, where the cirrus clouds reflect shortwave radiation due to the increased albedo (up to 230% for cirrus2 in comparison to the reference case!). We can observe the same phenomena than in the sections before, that cirrus clouds reflect in the solar regime, and absorb in the longwave regime.

Channel (μm)	RHi 100%	RHi 130%	Cirrus1	Cirrus2
1: 0.48 - 0.68	44.401	44.401	46.252	54.278
% of RHi 100%		99.999%	104.169%	122.245%
2: 0.725 - 1.00	48.379	48.379	50.711	60.815
% of RHi 100%		99.999%	104.821%	125.705%
3a: 1.58 - 1.64	0.192	0.192	0.241	0.443
% of RHi 100%		99.999%	125.455%	230.826%
3b: 3.55 - 3.93	0.139	0.139	0.147	0.168
% of RHi 100%		99.999%	105.919%	121.173%
4: 10.3 - 11-3	63.417	63.417	62.396	57.626
% of RHi 100%		99.999%	98.390%	90.868%
5: 11.5 - 12.5	67.216	67.216	66.009	60.642
% of RHi 100%		99.999%	98.204%	90.220%

Table 4.2: TOA outgoing radiation for the 6 different spectral bands of AVHRR in Wm^{-2} and the difference to the reference case (RHi 100%) in %

The impact for the IASI sensor is shown in table 4.3. Because we have assumed to take only the three main bands into consideration (without their spectral samples), the bands are much broader than those of the AHVRR.

This leads to the result, that the difference in the outgoing longwave radiation for the four cases does not vary allot (in respect to the spectral band). Again, the ISSR does not influence the outgoing radiation allot (maximum: 0.27%). The thin cirrus clouds decrease the outgoing longwave radiation by 98.6% (cirrus1, mean value) and 92.2% (cirrus2, mean value), where the strongest effect can be estimated for band 2.

Interval (μm)	RHi 100%	RHi 130%	Cirrus1	Cirrus2
1: 3.62 - 5.00	2.899	2.899	2.874	2.727
% of RHi 100%		99.999%	99.14%	94.078%
2: 5.00 - 8.26	23.693	23.629	23.282	21.597
% of RHi 100%		99.729%	98.264%	91.153%
3: 8.26 - 15.5	137.193	137.191	135.067	125.224
% of RHi 100%		99.999%	98.450%	91.276%

Table 4.3: TOA outgoing radiation for the 3 different spectral bands of IASI in Wm^{-2} and the difference to the reference case (RHi 100%) in %

For conclusion, it has to be considered, that for AVHRR/3 and IASI, ISSRs can be neglected, but thin cirrus clouds could be a source of error. To prevent this kind of errors in satellite data retrievals, thin cirrus clouds have to be detected precisely. This could be performed during the quality control procedures. For this purpose, the L2-MOD6 product of MODIS could be used to detect thin cirrus clouds with an optical depth > 0.02 (uncertainty factor 2!) (e.g. Dessler et al. (2002)). This case study should have shown, how important cloud clearing of also very thin clouds is.

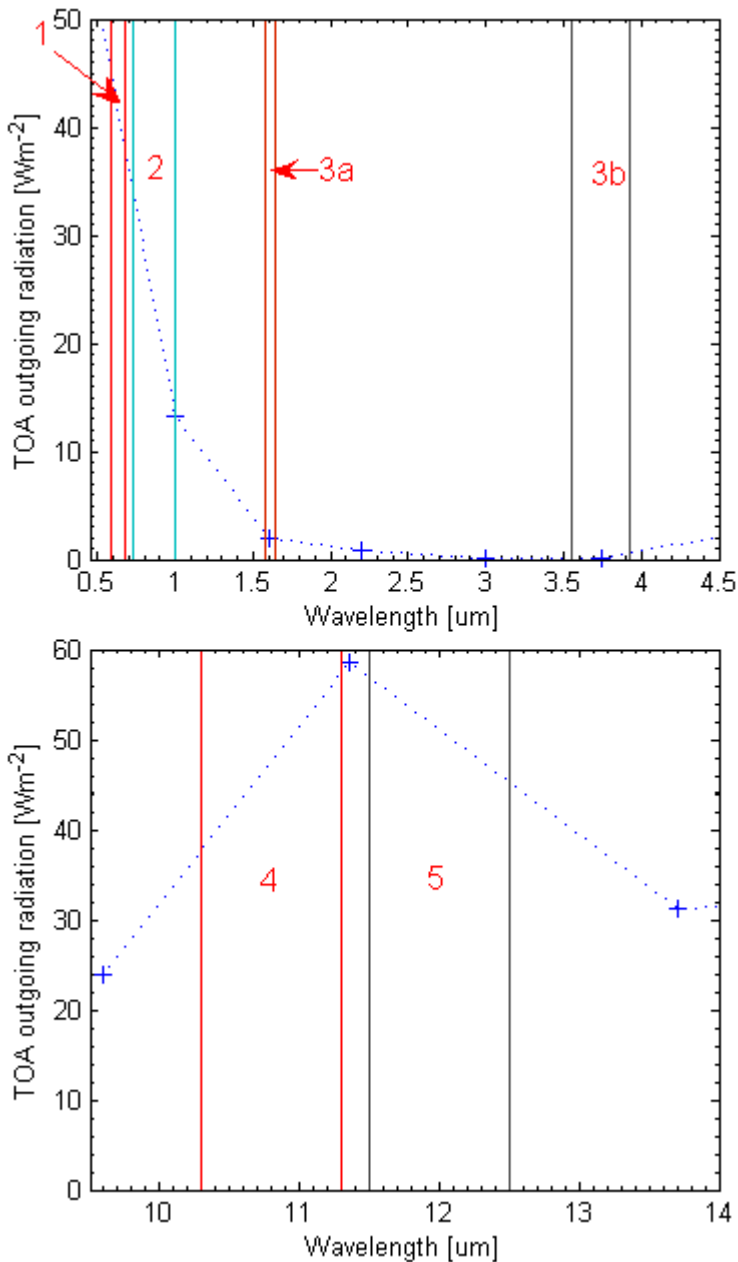


Figure 4.18: The spectral bands of the AVHRR/3, blue crosses stand for the total outgoing radiation of each spectral band of the radiation transfer model (in Wm^{-2}), reference case (RH_i 100%)

Chapter 5

Conclusions and Outlook

In this thesis I have investigated the impact of ISSRs and thin cirrus clouds on the radiation budget. For this purpose I used corrected radiosonde profiles for statistical investigations and constructed average supersaturation profiles with an supersaturated layer centered at the average altitude of 8200 m, with a vertical extension of 1200 m and a fixed but variable maximum relative humidity with respect to ice between 80 and 130%. This profiles were used in order to obtain the general features of the radiative properties of ice supersaturated regions and thin cirrus clouds containing ice supersaturation. Additionally, I investigated possible errors in remote sensing applications, using the spectral bands of AHVRR/3 and IASI.

From my investigations I could answer some questions concerning the radiative impact of ISSRs and thin cirrus clouds: (1) The impact of ice supersaturation on the surface is negligible. (2) There is a small effect on the outgoing longwave radiation due to ISSRs of up to $1Wm^{-2}$. (3) In the vertical profiles I found changes in the longwave heating rates up to 1 K/d for RH=130% compared to the saturated profiles. These changes in the heating rates could affect the local dynamics under certain conditions and could trigger the formation of thin cirrus clouds due to radiative cooling at the top of the supersaturated layer. (4) The radiative impact of (even) thin cirrus clouds is much stronger than for ISSRs and depends strongly on ice water content and ice crystal number concentration. In our calculations the optical depth can vary between 1.308 and 0.016, the values of OLR are between $188.9 Wm^{-2}$ and $250.4 Wm^{-2}$ and the reflected shortwave radiation reaches values between $129.5 Wm^{-2}$ and $199.9 Wm^{-2}$. For small number concentrations $N < 320 L^{-1}$ this causes in general a net warming in our scenarios whereas for larger crystal densities the shortwave cooling

dominates. (5) Incorrectly formed cirrus clouds can produce large errors in the integrated fluxes up to compared to as well as in the vertical profiles of the heating rates. (6) The local dynamic can be changed within hours due to destabilisation of the stratification. (7) The impact of ISSRs on the investigated remote sensing applications is very weak, but cirrus clouds can tremendously influence the measured radiation. I would recommend to use precise cloud clearing techniques.

A general estimate on the radiative impact of ISSRs and thin cirrus clouds as e.g. in Gettelman and Kinnison (2006) could not be derived, because we have only data from a location at the Northern hemisphere in the mid latitudes. However, we get a first impression of the radiative impact of ISSRs and thin cirrus clouds and possible errors in GCM due to non physical cirrus cloud parametrisation.

As we have seen, the radiative influence of ISSRs could lead to local changes in the vertical profiles of heating rates. For further investigations we will include a radiation transfer model into a cloud resolving cirrus cloud model (EULAG) to investigate the radiative impact on the vertical profiles and on the local dynamics.

Appendix

A - Derivation of the Effective Radius

For the definition of the effective radius of ice crystals, we try to use the concept of Ebert & Curry (1992) about polydispered, randomly oriented hexagonal cylinders. Peter Spichtinger developed following method, to solve the integrals in an analytical way using the momentum of the distribution. The effective radius is defined like this:

$$r_{eff} = \frac{\int_0^{\infty} \left(\frac{A}{4\pi}\right)^{3/2} \cdot f(L) dL}{\int_0^{\infty} \frac{A}{4\pi} \cdot f(L) dL} \quad (5.1)$$

Where A stands for the surface of a hexagonal cylinder. The cylinders are defined with a length L , and a diameter $D = 2a$. The area of a cylinder is constructed out of 6 equilateral triangles with an area $A_{\Delta} = \frac{3\sqrt{3}}{2}a^2$. It follows the area of the hexagon: $A_{hex} = 6 \cdot A_{\Delta}$. The whole surface and the volume of a hexagonal cylinder can now be constructed. Later we want to convert a in dependence of the mass, so we use the relation $V = \frac{m}{\rho_b}$ with the bulk depth ρ_b :

$$A = 2 \cdot A_{hex} + 6 \cdot a \cdot L = 6 \left(\frac{\sqrt{3}}{2}a^2 + a \cdot L \right)$$
$$V = A_{hex} \cdot L = \frac{3\sqrt{3}}{2}a^2L \Leftrightarrow a^2 = \frac{2}{3\sqrt{3}\rho_b} \cdot \frac{m}{L} \quad (5.2)$$

We use also the relation between mass and length with the coefficients α and β developed by Heymsfeld & Jaquinta (2000):

$$\frac{m}{m_0} = \alpha \cdot \left(\frac{L}{L_0}\right)^{\beta} \Leftrightarrow \frac{L}{L_0} = \frac{1}{\alpha^{1/\beta}} \cdot \left(\frac{m}{m_0}\right)^{1/\beta} \quad (5.3)$$

whereby the coefficients have following values:

$$\begin{aligned}\alpha &= 1.649 \cdot 10^{-3} \\ \beta &= 2.2 \\ \rho_b &= 0.81 \cdot 10^3 \frac{kg}{m^3} = 0.81 \frac{g}{cm^3}\end{aligned}$$

Now, the equation 5.2 using the relation 5.3 converts to:

$$a(L) = \sqrt{\frac{2m_0\alpha}{3\sqrt{3}\rho_b \cdot L_0}} \cdot \left(\frac{L}{L_0}\right)^{\frac{\beta-1}{\beta}} \quad (5.4)$$

$$a(m) = \sqrt{\frac{2m_0\alpha^{1/\beta}}{3\sqrt{3}\rho_b \cdot L_0}} \cdot \left(\frac{m}{m_0}\right)^{\frac{\beta-1}{2\beta}} \quad (5.5)$$

The aspect ration between the diameter and the length of the hexagonal cylinder is defined as: $r_a = \frac{L}{2a}$ ($\Leftrightarrow a = \frac{L}{2r_a}$). We can constitute now the equations 5.4 and 5.5 in the equation for r_a . After some conversions it follows:

$$r_a(L) = \frac{L_0}{\underbrace{\sqrt{\frac{8m_0\alpha}{3\sqrt{3}\rho_b \cdot L_0}}}_{L_m}} \cdot \left(\frac{L}{L_0}\right)^{\frac{3-\beta}{2}} = L_m \cdot \left(\frac{L}{L_0}\right)^{\frac{3-\beta}{2}} \quad (5.6)$$

$$r_a(m) = \frac{L_0}{\underbrace{\sqrt{\frac{8m_0\alpha^{3/\beta}}{3\sqrt{3}\rho_b \cdot L_0}}}_{R_m}} \cdot \left(\frac{m}{m_0}\right)^{\frac{3-\beta}{2\beta}} = R_m \cdot \left(\frac{m}{m_0}\right)^{\frac{3-\beta}{2\beta}} \quad (5.7)$$

We can substitute the diameter in the area-formula with r_a :

$$A = 3 \frac{L^2}{r_a} \left(1 + \frac{\sqrt{3}}{4r_a}\right) \quad (5.8)$$

Further, we need also a simplified expression for $A^{3/2}$. We can solve this with a taylor series:

$$(1+x)^{\frac{n}{m}} = 1 + \frac{n}{m}x - \frac{n(m-n)}{2! \cdot m^2}x^2 \pm \dots$$

With $n = 3$, $m = 2$ and $x = \frac{\sqrt{3}}{4r_a}$ it follows:

$$A^{3/2} \approx \sqrt{27} \frac{L^2}{r_a} \cdot \left(1 + \frac{\sqrt{27}}{8r_a} + \frac{9}{128r_a^2}\right)$$

We can now substitute $r_a(m)$ with the expression 5.7 and L with the expression 5.3:

$$\Rightarrow A(m) = \underbrace{\frac{3L_0^2}{R_m \alpha^{2/\beta}}}_{C_{21}} \cdot \left(\frac{m}{m_0}\right)^{\frac{\beta+1}{2\beta}} + \underbrace{\frac{\sqrt{27}L_0^2}{4R_m^2 \alpha^{2/\beta}}}_{C_{22}} \cdot \left(\frac{m}{m_0}\right)^{\frac{\beta-1}{\beta}} \quad (5.9)$$

$$\begin{aligned} \Rightarrow (A(m))^{3/2} &\approx \underbrace{\frac{\sqrt{27}L_0^3}{R_m^{3/2} \alpha^{3/\beta}}}_{C_{11}} \cdot \left(\frac{m}{m_0}\right)^{\frac{3(\beta+1)}{4\beta}} + \underbrace{\frac{27L_0^3}{8R_m^{5/2} \alpha^{3/\beta}}}_{C_{12}} \cdot \left(\frac{m}{m_0}\right)^{\frac{5\beta-3}{4\beta}} \\ &+ \underbrace{\frac{9\sqrt{27}L_0^3}{128R_m^{7/2} \alpha^{3/\beta}}}_{C_{13}} \cdot \left(\frac{m}{m_0}\right)^{\frac{7\beta-9}{4\beta}} \end{aligned} \quad (5.10)$$

We can transform our integral 5.1 to a mass dependent form using the relation $f(L) dL = f(m) dm$. It follows:

$$\begin{aligned} \int_0^\infty (A(m))^{3/2} f(m) dm &= \int_0^\infty C_{11} \left(\frac{m}{m_0}\right)^{\frac{3(\beta+1)}{4\beta}} f(m) dm \\ &+ \int_0^\infty C_{12} \left(\frac{m}{m_0}\right)^{\frac{5\beta-3}{4\beta}} f(m) dm \\ &+ \int_0^\infty C_{13} \left(\frac{m}{m_0}\right)^{\frac{7\beta-9}{4\beta}} f(m) dm \\ \int_0^\infty A(m) f(m) dm &= \int_0^\infty C_{21} \left(\frac{m}{m_0}\right)^{\frac{\beta+1}{2\beta}} f(m) dm \\ &+ \int_0^\infty C_{22} \left(\frac{m}{m_0}\right)^{\frac{\beta-1}{\beta}} f(m) dm \end{aligned}$$

The function $f(m)$ stands for the distribution of the mass, which is constructed as a lognormal-distribution:

$$f(m) = \frac{N}{\sqrt{2\pi} \cdot \log \sigma_m} \cdot \exp\left(-\frac{1}{2} \left(\frac{\log\left(\frac{m}{m_m}\right)}{\log \sigma_m}\right)^2\right)$$

$\rightarrow m_m$ stands in relation to the mean mass $\bar{m} = \frac{IWC}{N}$; $\bar{m} = m_m \cdot r^{1/2}$, where $r = 2.2$ is the width of the distribution. Using the relation $\sigma_m =$

$\exp(\sqrt{\log r}) \Leftrightarrow \log r = (\log \sigma_m)^2$, we can develop the mass distribution to:

$$\begin{aligned}\mu_k[m] &= N \cdot m_m^k \cdot \exp\left(\frac{1}{2}k^2 \cdot \log r\right) \\ &= N \cdot \bar{m}^k \cdot r^{\frac{k(k-1)}{2}}\end{aligned}\quad (5.11)$$

Finally, we can substitute the mass distribution in our integral with expression 5.11:

$$\begin{aligned}\int_0^\infty (A(m))^{3/2} f(m) dm &= C_{11} \cdot \mu_{\frac{3(\beta+1)}{4\beta}}[m] + C_{12} \cdot \mu_{\frac{5\beta-3}{4\beta}}[m] \\ &\quad + C_{13} \cdot \mu_{\frac{7\beta-9}{4\beta}}[m] \\ \int_0^\infty A(m) f(m) dm &= C_{21} \cdot \mu_{\frac{\beta+1}{2\beta}}[m] + C_{22} \cdot \mu_{\frac{\beta-1}{\beta}}[m]\end{aligned}$$

We can reformulate our equation for the effective radius (3.6) to:

$$r_{eff} \approx \frac{1}{2\sqrt{\pi}} \frac{C_{11} \cdot \mu_{\frac{3(\beta+1)}{4\beta}} + C_{12} \cdot \mu_{\frac{5\beta-3}{4\beta}} + C_{13} \cdot \mu_{\frac{7\beta-9}{4\beta}}}{C_{21} \cdot \mu_{\frac{\beta+1}{2\beta}} + C_{22} \cdot \mu_{\frac{\beta-1}{\beta}}}\quad (5.12)$$

For small ice crystals, we can make the assumption, that $L = 2a \rightarrow r_a = 1$. Using this simplification, we can reformulate the area terms to:

$$\begin{aligned}A &= \underbrace{\frac{3 \left(1 + \frac{\sqrt{3}}{4}\right) L_0^2}{\alpha^{2/\beta}}}_{D_1} \cdot \left(\frac{m}{m_0}\right)^{2/\beta} \\ A^{3/2} &= \underbrace{\frac{\left(3 \left(1 + \frac{\sqrt{3}}{4}\right)\right)^{3/2} L_0^3}{\alpha^{3/\beta}}}_{D_2} \cdot \left(\frac{m}{m_0}\right)^{3/\beta}\end{aligned}$$

$$\begin{aligned}\int_0^\infty A(m) f(m) dm &= D_2 \cdot \mu_{2/\beta}[m] \\ \int_0^\infty (A(m))^{3/2} f(m) dm &= D_1 \cdot \mu_{3/\beta}[m]\end{aligned}$$

$$\Leftrightarrow r_{eff,small} \approx \frac{D_1 \cdot \mu_{3/\beta}}{D_2 \cdot \mu_{2/\beta}}\quad (5.13)$$

We can also combine the r_{eff} for small crystals with the r_{eff} for large crystals using this approximation:

$$r_{eff,corr} = r_{eff} \cdot \left(1 - \exp \left(- \left(\frac{L \cdot r^{1.2}}{1.6 \cdot 10^{-4}} \right)^{0.46} \right) \right) \quad (5.14)$$

B - List of Abbreviations

IRE	ISSR radiative effect
ISSR	ice supersaturated region
IWC	ice water content
HR	heating rate
lw	longwave
N	ice crystal number density
OLR	outgoing longwave radiation
RH	relative humidity
RHi	relative humidity with respect to ice
RHw	relative humidity with respect to water
sat	saturated
SCM	single column model
SVC	subvisible cirrus
sw	shortwave
T	temperature
TOA	top of the atmosphere
UV	ultraviolet
uRHi	upper relative humidity wrt ice
wrt	with respect to

Bibliography

- Chen, T., W.B. Rossow, and Y. Zhang, 2000: Radiative Effects of Cloud-Type Variations. *Journal of Climate*, 13, 264-286.
- Clark, T., and R. Farley, 1984: Severe downslope windstorm calculations in two and three spatial dimensions using anelastic interactive grid nesting: A possible mechanism for gustiness. *Journal Atmospheric Science*, 41, 329-350.
- Comstock, J. M., T. P. Ackerman, and D. D. Turner, 2004: Evidence of high ice supersaturation in cirrus clouds using ARM Raman lidar measurements. *Geophysical Research Letters*, 31, L11106.
- DeMott, P., D. Cziczo, A. Prenni, D. Murphy, S. Kreidenweis, D. Thomson, R. Borys, and D. Rogers, 2003: Measurements of the concentration and composition of nuclei for cirrus formation. *Proceedings of the National Academy of Sciences*, 100 (25), 14655-14660.
- Dessler, A. E., and P. Yang, 2002: The Distribution of Tropical Thin Cirrus Clouds Inferred from Terra MODIS Data. *Journal of Climate*, 16, 12411247
- Dobbie, J.S., J.N. Li, and P. Chylek, 1999: Two- and four-stream optical properties for water clouds and solar wavelengths. *Journal of Geophysical Research*, 104, 2067-2079.
- Ebert, E.E., and J.A. Curry, 1992: A parametrization of ice cloud optical properties for climate models. *Journal of Geophysical Research*, 97, 3831-3836.
- Forster, de F.P., and J.M. Gregory, 2006: The Climate Sensitivity and Its Components Diagnosed from Earth Radiation Budget Data. *Journal of Climate*, 19, 39-52.

- Fu, Q.A.: An accurate parameterization of the solar radiative properties of cirrus clouds for climate models, *Journal of Climate*, 9, 2058-2082.
- Fu, Q.A., P. Yang, and W. B. Sun, 1998: An accurate parameterization of the infrared radiative properties of cirrus clouds for climate models, *Journal of Climate*, 11, 2223-2237.
- Gottelman, A., V.P. Walden, L.M. Miloshevich, W.L. Roth, and B. Halter, 2006: Relative humidity over Antarctica from radiosondes, satellites, and a general circulation model. *Journal of Geophysical Research*, 111 (D9), D09S13.
- Gottelman, A., and D.E. Kinnison, 2006: The global impact of supersaturation in a coupled chemistry-climate model. *Atmospheric Chemistry and Physics Discussions*, 6, 12433-12468.
- Gierens, K., and P. Spichtinger, 2000: On the size distribution of ice supersaturation regions in the upper troposphere and lower stratosphere. *Annales Geophysicae*, 18, 499-504.
- Glückauf, E., 1945: Notes on upper air hygrometry-II: On the humidity in the stratosphere. *Royal Meteorological Society - Quarterly Journal*, 71, 110-112.
- Halthore, R. N., S. E. Schwartz, J. J. Michalsky, G. P. Anderson, R. A. Ferrare, B. N. Holben, and H. Ten Brink, 1997b: Comparison of model estimated and measured direct-normal solar irradiance. *Journal of Geophysical Research*, 102, 29,991 - 20,002.
- Heymsfield, A.J., and J. Iaquinta, 2000: Cirrus crystal terminal velocities. *Journal of Atmospheric Science*, 57, 916-938.
- Jawitz, J.W., 2004: Moments of truncated continuous univariate distributions. *Advances in Water Resources*, 27 (3), 269-281.
- Jensen, E.J., O.B. Toon, A. Tabazadeh, G.W. Sachse, B.E. Anderson, K.R. Chan, C.W. Twohy, B. Gandrud, S.M. Aulenbach, A. Heymsfield, J. Hallett, and B. Gary, 1998: Ice nucleation processes in upper tropospheric wave-clouds during SUCCESS. *Geophysical Research Letters*, 25, 1363-1366.
- Kärcher, B., and U. Lohmann, 2002: A parameterization of cirrus cloud formation: Homogeneous freezing of supercooled aerosols. *Journal of Geophysical Research*, 107, 10.1029/2001JD000470.

- Koop, T., B. Luo, A. Tsias, and T. Peter, 2000: Water activity as the determinant for homogeneous ice nucleation in aqueous solutions. *Nature* 406, 611-614.
- Leiterer U., H. Dier, D. Nagel, T. Naebert, D. Althausen, K. Franke, A. Kats, and F. Wagner, 2005: Correction method for RS80-A humidity profiles and their validation by lidar backscattering profiles in tropical cirrus clouds. *Journal of Atmospheric and Oceanic Technology*, 22 (1), 18-29.
- Lohmann, U. and B. Kärcher, 2002: First interactive simulations of cirrus clouds formed by homogeneous freezing in the ECHAM GCM. *Journal Geophysical Research*, 107, 4105, doi:10.1029/2001JD000767.
- Lohmann, U., N. McFarlane, L. Levkov, K. Abdella, and F. Albers, 1999: Comparing different cloud schemes of a single column model by using mesoscale forcing and nudging technique. *Journal of Climate*, 12, 438-461.
- Marenco, A., P. v. Thouret, H. Nedelec, H. Smit, M. Helten, H. Karcher, P. Simon, K. Law, J. Pyle, G. Poschmann, R. van Wrede, C. Hume, and T. Cook, 1998: Measurement of ozone and water vapor by Airbus in-service aircraft: the MOZAIC airborne program, an overview. *Journal of Geophysical Research*, 103(D19), 25,631-25,642.
- Molina, L.T., and M.J. Molina, 1986: Absolute absorption cross sections of ozone in the 185- to 350-nm wavelength range. *Journal of Geophysical Research*, 91, 14501-14508.
- Ovarlez, J., P. van Velthoven, G. Sachse, S. Vay, H. Schlager, and H. Ovarlez, 2000: Comparison of water vapor measurements from POLINAT 2 with ECMWF analyses in high humidity conditions. *Journal of Geophysical Research*, 105, 3737-3744.
- Ovarlez, J., J.-F. Gayet, K. Gierens, J. Ström, H. Ovarlez, F. Auriol, R. Busen, U. Schumann, 2002: Water vapor measurements inside cirrus clouds in northern and southern hemispheres during INCA. *Geophysical Research Letters*, 10.1029/2001GL014440.
- Peter, T., C. Marcolli, P. Spichtinger, T. Corti, M.B. Baker, and T. Koop, 2006: When dry air is too humid. *Science* 314 (5804), 1399-1400.
- Quante, M., 2004: The role of clouds in the climate system. *Journal de Physique IV*, 121, 61-86.

- Schumann, U., D.K. Lynch, K. Sassen, D. Starr, and G. Stephens 2002: Contrail Cirrus. Oxford University Press, 231-255.
- Slingo, A., 1989: A GCM parameterization for the shortwave radiative properties of water clouds. *Journal of Atmospheric Science*, 46, 1419-1427.
- Smolarkiewicz, P., and L. Margolin, 1997: On forward- in-time differencing for fluids: an Eulerian/Semi- Lagrangian non-hydrostatic model for stratified flows. *Atmosphere-Oceans*, 35, 127-152.
- Soden, B.J., D.L. Jackson, V. Ramaswamy, M.D. Schwarzkopf, and X.L. Huang, 2005: The radiative signature of upper tropospheric moistening. *Science* 310 (5749), 841-844.
- Sonntag, D., 1994: Advancements in the field of hygrometry. *Meteorologische Zeitschrift*, 3, 51-66.
- Spichtinger, P., K. Gierens, U. Leiterer, and H. Dier, 2003a: Ice supersaturation in the tropopause region over Lindenberg, Germany. *Meteorologische Zeitschrift*, 12, 143-156.
- Spichtinger, P., K. Gierens, and W. Read, 2003b: The global distribution of ice supersaturated regions as seen by the microwave limb sounder. *Royal Meteorological Society - Quarterly Journal*, 129, 3391-3410.
- Spichtinger, P., K. Gierens, H.G.J. Smit, J. Ovarlez, and J.-F. Gayet, 2004: On the distribution of relative humidity in cirrus clouds. *Atmospheric Chemistry and Physics Discussions*, 4, 639-647.
- Spichtinger, P., Gierens K., and H. Wernli, 2005: A case study on the formation and evolution of ice supersaturation in the vicinity of a warm conveyor belt's outflow region. *Atmospheric Chemistry and Physics*, 5, 973-987.
- Tompkins, A., K. Gierens, and G. Radel, 2007: Ice supersaturation in the ECMWF integrated forecast system. *Royal Meteorological Society - Quarterly Journal*, in press.
- Vay, S.A., B.E. Anderson, E.J. Jensen, G.W. Sachse, J. Ovarlez, G.L. Gregory, S.R. Nolf, J.R. Podolske, T.A. Slate, and C.E. Sorenson, 2000: Tropospheric water vapor measurements over the North Atlantic during the Subsonic Assessment Ozone and Nitrogen Oxide Experiment (SONEX). *Journal Geophysical Research*, 105, 3745-3756.

Wall, E., 1942: Material zur Frage der Eiskeimbildung in der Atmosphäre. *Meteorologische Zeitschrift*, 59(4), 109-120.

Zhang, J.H., U. Lohmann, and P. Stier, 2005: A microphysical parameterization for convective clouds in the ECHAM5 climate model: Single-column model results evaluated at the Oklahoma Atmospheric Radiation Measurement Program site. *Journal of Geophysical Research*, 110 (D15), D15S07.